A novel approach for modelling stress fields induced by shallow water flows on movable beds

Alia Al-Ghosoun[a,*], Mohammed Seaid[b], Ashraf S. Osman[b]

[a]*Department of Mechatronics Engineering, Philadelphia University, Amman, Jordan*
[b]*Department of Engineering, University of Durham, South Road, DH1 3LE, United Kingdom*

Abstract

Sediment transport in shallow waters occurs when the water flows over the bed for which the amount of generated sediments can be determined from the transport mechanism caused by the consequent flow. Recently, investigating the bedload and sediment transport using numerical models has been rapidly increased and various techniques have been developed to quantify both the hydrodynamics and morphodynamics in these systems but not the stress distributions in the deformed beds. In the present study, we propose a novel class of coupled finite element/finite volume methods to resolve the effect of sedimentary shallow water flows on the internal stresses in bed topographies. The coupled model employs the linear elasticity for the bed and the nonlinear shallow water equations for the water flow. Suspended sediments are also taken into consideration in this study, and impacts of the erosion and deposition are modelled using well-established empirical equations. The linear equations of elasticity are solved numerically using a finite element approach on unstructured meshes, while the nonlinear shallow water equations are numerically solved using a well-balanced finite volume method. We also introduce an accurate algorithm to sample forces on the interface between the water flow and bed topography to be implemented as coupling conditions between finite volume cells and finite element nodes. Distributions of stress fields in the bed topography due to erosion and sediment transport by shallow water flows are presented for several test examples. The novel coupled model is stable, efficient, accurate, well-balanced and it can be used for solving complex geometries. In addition, the proposed approach offers significant advancements in understanding sedimentary processes in shallow water environments and the induced underground stresses as a result of these processes.

Keywords: Sediment transport; Erodible beds; Stress analysis; Linear elasticity; Shallow water equations; Finite element method; Finite volume method.

1. Introduction

In recent years, increasing emphasis has been dedicated to the modelling and simulation of erosion/deposition characteristics in bed topographies by water flows since the knowledge of factors influencing erosion is useful in the design of drainage, road cuts, embankments, ditches and other surfaces, see for example [1]. In fact, it is very important to develop a complete understanding of stresses distributions in bed topographies due to erosion by water flows to avoid failure such as during the installation of driven piles, see [2] among others. In this case, it is crucial getting the sediment mass around the pile to resist the erosion and deposition effects. The complexity of this class of sediment-failure models and the additional testing required to determine the different involved sediment parameters, minimize their utility for geotechnical engineers in practice. Understanding the dynamics of erosion/deposition patterns and sediment transport is also vital to predict the changes in coastal dynamics and evaluate the performance of coastal structures [3]. It should be noted that the main goal of sediment transport analysis is to determine changes in the bed level over time for the hydrodynamic systems including bays, rivers, estuaries, and other near-shore areas where water

*Corresponding author
Email addresses: aalghsoun@philadelphia.edu.jo (Alia Al-Ghosoun), m.seaid@durham.ac.uk (Mohammed Seaid), ashraf.osman@durham.ac.uk (Ashraf S. Osman)

flow and bed topography interact [4]. Hence, the sediment stresses resulting from the erosion and deposition are of paramount importance to geotechnics because it is a driver of geotechnical changes in soils. These stresses can also be used to describe the forces applied to the topography surfaces which are transmitted into the bed to exert internal shear stresses that result in the sediment deformation or fractures [5]. Furthermore, the sediment transport is an important step in the process of soil erosion which depends on several hydraulic parameters including the mean flow velocity, unit discharge and slope gradient, see for instance [6]. This requires a quantitative understanding of the relation between characteristics of the water flow and the fundamental sediment properties [7]. Many experimental techniques have also been developed to quantify different parameters in sediment transport problems [8], as it is generally recognized that chemical, biological, and physical factors have a significant impact on the strength of the intertidal mud flat. Nevertheless, it is not possible to assess these factors independently and forecast the bed strength with any degree of accuracy [9]. Measuring the critical shear stress for erosion in the bed top layer is one of the well-established treatments for this problem. This technique allows for the reconstruction of all the shear strength parameters within the same overall parameter [10]. In practice, critical shear stress of the erosion, defined as the maximum shear strength of the bed top layer, can be evaluated in the laboratory. However, these experimental tests tend to not properly reflect the conditions of in-situ bed topographies. For instance, to qualitatively analyze the interactions between the eroded bed resulting from the hydraulic processes and its deposition in the river, a flume test was employed in [8]. The coupling relationship between the eroded bed and its transport and deposition in the river bed has also been studied in [11] using a curved channel flume. The cohesive sediment experiences significant changes in sediment properties during its storage, transportation, core, and laboratory analysis. These changes can significantly alter effects of the sediment, despite physical experiments can qualitatively measure the amounts of material eroded and deposited within the close domain [12]. Recently, different methodologies have been improved to address the challenge of developing stable and accurate numerical methods for solving erosion/deposition effects in shallow water flows. Most of these approaches employ approximate [13] or exact [14] forms of the eigenvalues of the Jacobian matrix associated with the considered mathematical model. In [15], a first-order HLLC scheme was proposed and a wave-speed estimator was provided for the Exner equation. The obtained results were affected by the numerical diffusion and fine meshes were required to achieve accurate results. In [16], a finite volume method based on the Roe-type solvers was implemented for solving shallow water waves over mobile beds. It has been shown in this reference that stable numerical results can be obtained without the use of the computationally demanding schemes using the coupled Jacobian matrix. The numerical study of a sudden erosional flow initiated by the release of a dam-break wave over a loose sediment bed was also investigated in [17] using a Riemann solver.

Development of accurate description of fundamental sediment transport processes such as transport of solid particles in suspension, erosion and deposition is vital in developing a reliable numerical model to simulate dynamics of the cohesive sediment transport. A study has been carried out in [18] to examine the stability of cohesive river banks by determining the ratio of the driving forces to provide resistance on the collapse surface and it introduced a hypothetical collapse model to be associated with the cohesive river banks. However, this model and the one investigated in [6] neglect the impact of tensile fractures and hydrostatic pressure. As a consequence, an improved collapse model has been proposed in [19] for the cohesive river banks which takes into account these effects of tensile cracks and it assumes that the collapsed surface passes through the foot of bank slope. In [20], an augmented Roe approach was implemented for the simulation of bedload transport using the shallow water equations coupled to a mass conservation equation for the bed layer. A numerical model for depth-integrated hyper-concentrated and mud/debris shallow flows, including variable-density and non-uniform solid-phase transport was also presented in [21]. The resulting system of equations is formed by the conservation laws for the mass and momentum of the mixture, supplemented by the mass conservation equation for the different sizes of suspended sediments in the water flow. In the present study, we propose a fully coupled model for stress recovery in the bottom topographies induced by shallow water flows on movable beds. The governing equations consist of the one-dimensional nonlinear hydro-morphodynamic system for the water flow and bedload transport whereas for the bed deformation, the two-dimensional linear elasticity model has been implemented. The coupled model also involves empirical equations for erosion, deposition and bedload along with consistent transfer conditions at the interface between the solid bed and the water flow. As reported for shallow water waves by static elastic deformations in [22, 23], distributions of frictional terms and the hydrostatic pressure are used to sample horizontal and vertical forces at the interface between bed topographies and water bodies. Here, the deformation in the bed topography is due to the frictional force and hydrostatic pressure distribution resulting from the sediment transport and bedload. As a numerical solution for the coupled system, we use a well-balanced finite volume

method to solve the sediment transport by shallow water flows and an unstructured finite element method for the stress analysis. In addition, using a semi-implicit spatial integration of the bed friction in wet/dry control volumes on the interface, we provide a new treatment of wet/dry fronts in the finite volume solution of sediment transport. Coupling conditions at the interface are also investigated in this study for which a robust procedure for sampling forces and transferring them from finite volume cells to finite element nodes are implemented. The performance of the proposed coupled finite volume/element method is assessed using three well-established problems of sediment transport for which experimental measurements of the free-surface and bed profiles are available. Numerical results presented in this study demonstrate high resolution of the coupled finite volume/element method and confirm its capability to provide efficient and accurate simulations for stress fields induced by shallow water flows over deformed beds including erosion and deposition effects. It should also be stressed that while general efforts have been concentrated to present efficient numerical tools that allow solving sediment transport, to the best of our knowledge, stress distributions in the bed topography for these models have not been considered.

The rest of the paper is organized as follows. Formulation of the coupled model for shallow water sediment transport and the induced stresses is presented in section 2. Section 3 is devoted to the implementation of the numerical methods used for the solution procedure. We consider a two-dimensional finite element method for the bed deformations whereas a well-balanced finite volume method is implemented for the sediment transport. In section 4, we present numerical results and examples for stress fields induced by shallow water flows on movable beds. Our new approach is shown to enjoy the expected accuracy as well as the stability. Concluding remarks are summarized in section 5.

2. Governing equations for the coupled model

In the current work, we suppose that the vertical component of the acceleration is negligible, the water flow is almost horizontal, the pressure is hydrostatic, the gravity waves at the free surface are very long with respect to both the mean flow depth and the wave amplitude, and the mixture of water species is non-reactive and vertically homogeneous. In order to account for the accumulation of mass, resulting forces, and species within the control volume, the considered governing equations are therefore derived by balancing the net inflow of mass, momentum, and species through boundaries of a control volume during an infinitesimal time interval, see for example [24] and further details are therein. In general, the model consists of momentum and mass conservation equations for the water-sediment mixture and a set of mass conservation laws for bed and sediment materials. Hence, the equations governing the mass conservation and the momentum flux balance are

$$\begin{aligned} \frac{\partial h}{\partial t} + \frac{\partial (hv)}{\partial x} &= \frac{\mathcal{E} - \mathcal{D}}{1-p}, \\ \frac{\partial (hv)}{\partial t} + \frac{\partial}{\partial x}\left(hv^2 + \frac{1}{2}gh^2\right) &= -gh\frac{\partial Z}{\partial x} - \frac{(\rho_s - \rho_w)}{2\rho}gh^2\frac{\partial c}{\partial x} - \frac{(\rho_0 - \rho)(\mathcal{E} - \mathcal{D})v}{\rho(1-p)} - gh\tau_f, \end{aligned} \tag{1}$$

where x is the horizontal spatial coordinate, t the time variable, $h(t, x)$ the water depth, $Z(t, x)$ the bottom topography, $v(t, x)$ the depth-averaged water velocity, g the gravitational acceleration, p the porosity, ρ_w the water density, ρ_s the sediment density, c the depth-averaged concentration of the suspended sediment, $\mathcal{D}$ and $\mathcal{E}$ are the deposition and entrainment terms in downward and upward directions, respectively. In (1), $\rho(t, x)$ and ρ_0 are respectively, the density of the water–sediment mixture and the density of the saturated bed defined as

$$\rho = \rho_w(1 - c) + \rho_s c, \qquad \rho_0 = \rho_w p + \rho_s(1 - p), \tag{2}$$

whereas τ_f represents the friction force involving the Manning roughness coefficient M_b as

$$\tau_f = \frac{M_b^2 v\,|v|}{h^{1/3}}. \tag{3}$$

For modelling the mass conservation of species, we use the transport equation

$$\frac{\partial (hc)}{\partial t} + \frac{\partial (hvc)}{\partial x} = \mathcal{E} - \mathcal{D}, \tag{4}$$

and the bedload is updated using the following equation

$$\frac{\partial Z}{\partial t} = -\frac{\mathcal{E} - \mathcal{D}}{1 - p}. \tag{5}$$

Note that the entrainment flux $\mathcal{E}$ is mainly used to model the amount of bed sediment eroded into the water flow due to the turbulence which is then transported by the flow, whilst the deposition flux $\mathcal{D}$ models the deposition of this entrained sediment due to the gravity [25]. Although there are various formulae for modelling deposition and entertainment which were empirically proposed based on fieldwork datasets or laboratory, none can be universally applied due to the range and varying distribution of grain sizes. In the present study, we assume a non-cohesive sediment and we use the empirical relation reported in [26] as

$$\mathcal{D} = \omega \alpha_c (1 - \alpha_c c)^m c, \tag{6}$$

where ω is the settling velocity of a single particle in tranquil water defined by [27]

$$\omega = \sqrt{\left(\frac{13.95\mu}{\rho_w d_s}\right)^2 + 1.09 s g d_s} - \frac{13.95\mu}{\rho_w d_s}, \tag{7}$$

with μ is the dynamic viscosity of the water, d_s the averaged diameter of the sediment particles, and s the submerged specific gravity of sediment given by

$$s = \frac{\rho_s}{\rho_w} - 1.$$

In (6), m is an exponent indicating the effects of delayed settling due to high sediment concentrations and it is evaluated using the Reynolds number of the particles as

$$m = 4.45 Re^{-0.1}, \quad \text{with} \quad Re = \frac{\omega \rho_w d_s}{\mu}. \tag{8}$$

It should be mentioned that in order to guarantee that the concentration around the bed is not higher than the value of $(1 - p)$, the coefficient α_c in (6) is computed according to [28] by

$$\alpha_c = \min\left(2, \frac{1 - p}{c}\right).$$

For modelling the entrainment flux $\mathcal{E}$, we consider the formulation presented in [26] which makes use of a turbulent bursting outer-scale based function. This equation has also been implemented by other researchers [29, 30, 31, 32] to calculate the entrainment flux for dam-break flows over erodible sediment beds. A simplified version of this formulation is also presented in [33] as

$$\mathcal{E} = \begin{cases} \varphi \dfrac{\theta - \theta_{cr}}{h} \nu d_s^{-0.2}, & \text{if} \quad \theta \geq \theta_{cr}, \\ 0, & \text{otherwise}, \end{cases} \tag{9}$$

where φ is a coefficient used to control the erosion forces and it is determined by

$$\varphi = \varphi_c \frac{560\,(1 - p)\,\nu^{0.8}}{3\,(sg)^{0.4}\,\theta_{cr}}, \tag{10}$$

with φ_c is a value that depends on the phenomenon to be simulated. Notice that the exponent m and the coefficient φ were assumed constants in [26] however, to extend the applicability of our presented approach we consider a more general formulation of these coefficients which cover a wide spectrum of erosion/deposition applications. Needless to mention that the approach proposed in this study can accommodate other empirical expressions of erosion and

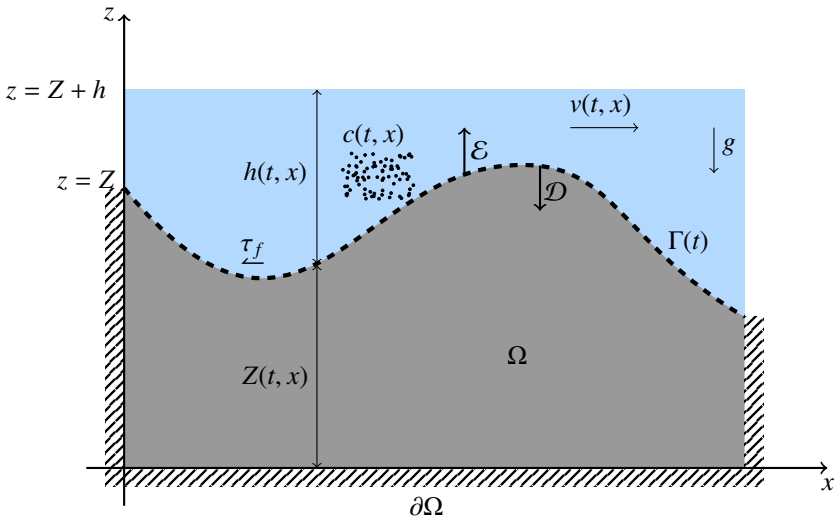

Figure 1: Illustration of the coupled system used for modelling stress fields induced by shallow water flows on movable beds.

deposition terms without any major conceptual modifications. Here, θ_{cr} is a critical value of Shields parameter for the initiation of the sediment motion and θ is the Shields coefficient defined by

$$\theta = \frac{v_*^2}{sgd}, \tag{11}$$

with v_* is the friction velocity defined using the Darcy-Weisbach factor f as [27]

$$v_* = \sqrt{\frac{f}{8}|v|}. \tag{12}$$

Note that using this formula for the entrainment flux $\mathcal{E}$, the initiation of motion for a sediment particle is expected to occur when a non-dimensionalization of the shear stress defined by the Shields parameter θ, reaches a value above the given critical threshold θ_{cr}. It should also be noted that the above equations involve different parameters in their formulations which need calibration accordingly. This calibration process is among the difficulties related to modelling sediment transport as it is problem-dependent and should be carried out to obtain the optimal values of the parameters involved in the empirical formulae used for the erosion and deposition terms. In the present study, this step has also been performed for the example with experimental measurements but not reported here for brevity in the presentation.

For ease of representation, we reformulate the sediment transport equations (1), (4) and (5) in a conservative form as

$$\frac{\partial \mathbf{W}}{\partial t} + \frac{\partial \mathbf{F}(\mathbf{W})}{\partial x} = \mathcal{Q}(\mathbf{W}) + \mathcal{R}(\mathbf{W}) + \mathcal{S}(\mathbf{W}), \tag{13}$$

where the vector of unknowns $\mathbf{W}$, the flux vector $\mathbf{F}(\mathbf{W})$ and the differential source terms $\mathcal{Q}(\mathbf{W})$ are

$$\mathbf{W} = \begin{pmatrix} h \\ hv \\ hc \\ Z \end{pmatrix}, \qquad \mathbf{F}(\mathbf{W}) = \begin{pmatrix} hv \\ hv^2 + \frac{1}{2}gh^2 \\ hvc \\ 0 \end{pmatrix}, \qquad \mathcal{Q}(\mathbf{W}) = \begin{pmatrix} 0 \\ -gh\frac{\partial Z}{\partial x} - \frac{(\rho_s - \rho_w)}{2\rho}gh^2\frac{\partial c}{\partial x} \\ 0 \\ 0 \end{pmatrix},$$

whereas the non-differential source vectors $\mathcal{R}(\mathbf{W})$ and $\mathcal{S}(\mathbf{W})$ are defined as

$$\mathcal{R}(\mathbf{W}) = \begin{pmatrix} \dfrac{\mathcal{E}-\mathcal{D}}{1-p} \\ -\dfrac{(\rho_0-\rho)(\mathcal{E}-\mathcal{D})v}{\rho(1-p)} \\ \mathcal{E}-\mathcal{D} \\ -\dfrac{\mathcal{E}-\mathcal{D}}{1-p} \end{pmatrix}, \qquad \mathcal{S}(\mathbf{W}) = \begin{pmatrix} 0 \\ -g\dfrac{M_b^2 v|v|}{h^{1/3}} \\ 0 \\ 0 \end{pmatrix}.$$

The system (13) is hyperbolic with four real eigenvalues λ_k ($k = 1, 2, 3, 4$) given by

$$\lambda_1 = 0, \qquad \lambda_2 = v, \qquad \lambda_3 = v - \sqrt{gh}, \qquad \lambda_4 = v + \sqrt{gh}. \tag{14}$$

Note that, in the characteristic analysis, the eigenvalues are determined primarily by the physical properties directly affecting the wave propagation and mass transport, such as the flow velocity v and the water depth h. The density ρ does not explicitly appear in the eigenvalues because the characteristic speeds are derived from the conservation laws (mass, momentum) and physical properties (gravity, flow velocity) of the water-sediment mixture, rather than directly from the density itself. However, the density appears in the corresponding eigenvectors and it influences the system dynamics through its role in governing the fluxes and interactions within the equations, but its variability across the domain does not directly alter the speeds at which disturbances propagate through the water flow.

In the present study, we are interested in the evaluation of stress fields generated in the bed topography due to the considered sediment transport model. To this end, an additional set of equations is required for the stress analysis in the xz-plane as illustrated in Figure 1. Assuming an isotropic elastic bed topography subject to external forces f_x and f_z in the x- and z-direction, respectively, the constitutive relations are given by [34]

$$\begin{aligned} \frac{\partial \sigma_x}{\partial x} + \frac{\partial \tau_{xz}}{\partial z} &= f_x, \\ \frac{\partial \sigma_z}{\partial z} + \frac{\partial \tau_{xz}}{\partial x} &= f_z, \end{aligned} \tag{15}$$

where τ_{xz} is the shear stress, σ_x and σ_z are the normal stress components in the x- and z-direction, respectively. In (15), $\mathbf{u} = (u_x, u_z)^\top$ is the displacement and $\boldsymbol{\epsilon}$ is the infinitesimal strain tensor defined as

$$\boldsymbol{\epsilon} = \frac{1}{2}\Big(\nabla\mathbf{u} + (\nabla\mathbf{u})^\top\Big). \tag{16}$$

As for many applications in linear elasticity, we consider the following constitutive stress-strain relation

$$\boldsymbol{\sigma} = \mathbf{D}\,\boldsymbol{\epsilon}, \tag{17}$$

where the stress vector $\boldsymbol{\sigma}$ and the constitutive matrix $\mathbf{D}$ are defined by

$$\boldsymbol{\sigma} = \begin{pmatrix} \sigma_x \\ \sigma_z \\ \tau_{xz} \end{pmatrix}, \qquad \mathbf{D} = \frac{E}{(1+\nu)(1-2\nu)} \begin{pmatrix} 1-\nu & \nu & 0 \\ \nu & 1-\nu & 0 \\ 0 & 0 & \dfrac{1-2\nu}{2} \end{pmatrix},$$

with E is the Young's modulus and ν is the Poisson's ratio characterizing the bed material. In (15), the forces f_x and f_z are generated by the erosion/deposition processes which occur on the bed due to the sediment transport and their explicit expressions are given in the next section. Here, the equations (15) are solved in a two-dimensional bounded domain Ω with a boundary $\partial\Omega$ and an interfacial boundary Γ between the water flow and the bed topography as shown in Figure 1. Notice that the interface Γ between the water and bed varies within the time such that

$$\Gamma(t) = \Big\{(x, z) \in \Omega : \quad z = Z(t, x)\Big\}.$$

On the boundaries, we use the following conditions

$$\begin{aligned} \boldsymbol{\sigma} \cdot \mathbf{n} &= 0, \qquad \text{on} \quad \Gamma, \\ \mathbf{u} &= \mathbf{0}, \qquad \text{on} \quad \partial\Omega \backslash \Gamma, \end{aligned} \tag{18}$$

where $\mathbf{n}$ is the outward unit normal on Γ. Note that the above conditions ensure that Γ is the only moving boundary part in the domain while all remaining parts are fixed solid walls. The deformation in the domain Ω is due to the applied forces f_x and f_z on the boundary Γ obtained from the sediment transport model. Note that other boundary conditions can also be incorporated in our system without major conceptual modifications. The coupled system is solved using a splitting operator where equations for stress analysis and equations for sediment transport are computed separately using the two-dimensional elastostatic equations (15) and the one-dimensional sediment transport equations (13), respectively. The coupling between the two models is achieved through the interface Γ by updating the bed topography $Z(t, x)$ at each time step and applying frictional forces f_x and f_z generated from the sediment transport on the boundary Γ. These interchange conditions are passed from the bed topography to the water flow and back during the time process.

3. Hybrid finite volume/finite element solver

To solve the coupled equations for the considered sediment transport and elastostatic model we propose a hybrid finite volume/finite element solver for which transfer conditions are transmitted on the interface Γ between the bed topography and the water flow at each time step. Here, the sediment transport equations are solved using a well-balanced finite volume method, and the elasticity equations are solved using an unstructured two-dimensional finite element method. In this section, we also discuss the discretization of source terms and the wet/dry treatment in the sediment transport equations along with the coupling conditions on the water-bed interface.

3.1. Finite volume solution of sediment transport

For the numerical solution of the sediment transport model (13), the finite volume method first proposed in [29] is adopted in the present work. The method employs a class of flux-limiter schemes using the second-order Lax–Wendroff method and a first-order Roe method. The method has been applied in [29] for solving dam-break flows over erodible beds and it produced highly accurate results without nonphysical oscillations and excessive numerical dissipation. However, as reported in [29], the method suffers from numerical instabilities requiring very small time steps to be used in the simulations, it also fails to resolve strong friction terms, and it is not suitable for flows over dry beds. To overcome these drawbacks, we propose in the present study new techniques to improve the numerical stability of the method and to allow for strong friction forces and wet/dry fronts in the simulations. Thus, unlike the previous work [29], the stability of the finite volume method is improved by adopting a splitting operator for the time integration along with a third-order Runge-Kutta method. For the spatial discretization of the system (13), we discretize the spatial domain into a set of control volumes $[x_{i-\frac{1}{2}}, x_{i+\frac{1}{2}}]$ with uniform size $\Delta x = x_{i+\frac{1}{2}} - x_{i-\frac{1}{2}}$ and $x_i = (i + \frac{1}{2})\Delta x$ is the center of the control volume. Integrating the system (13) with respect to space over the control volume $[x_{i-\frac{1}{2}}, x_{i+\frac{1}{2}}]$, we obtain the semi-discrete equations

$$\frac{d\mathbf{W}_i}{dt} + \frac{\mathcal{F}_{i+\frac{1}{2}} - \mathcal{F}_{i-\frac{1}{2}}}{\Delta x} = \mathcal{Q}(\mathbf{W}_i) + \mathcal{R}(\mathbf{W}_i) + \mathcal{S}(\mathbf{W}_i), \tag{19}$$

where $\mathbf{W}_i(t)$ is the space-averaged approximation of the solution $\mathbf{W}$ in the control volume $[x_{i-\frac{1}{2}}, x_{i+\frac{1}{2}}]$ at time t defined by

$$\mathbf{W}_i(t) = \frac{1}{\Delta x} \int_{x_{i-\frac{1}{2}}}^{x_{i+\frac{1}{2}}} \mathbf{W}(t, x)\, dx,$$

and $\mathcal{F}_{i\pm\frac{1}{2}} = \mathbf{F}(\mathbf{W}_{i\pm\frac{1}{2}})$ are the numerical fluxes in the cell interfaces $x = x_{i\pm\frac{1}{2}}$ at time t to be reconstructed in each control volume. For the time integration of the semi-discrete equations (19), the time domain is divided into subintervals $[t_n, t_{n+1}]$ with length $\Delta t_n = t_{n+1} - t_n$ and we use the notation W^n to denote the value of a generic function W at time t_n. Hence, the proposed splitting operator consists of the following three steps:

Step 1:

$$\begin{aligned} \frac{d\mathbf{W}_i^*}{dt} &= \mathcal{R}(\mathbf{W}_i^*), \qquad t \in (t_n, t_{n+1}], \\ \mathbf{W}_i^*(t_n) &= \mathbf{W}_i(t_n). \end{aligned} \tag{20}$$

Step 2:

$$\begin{aligned} \frac{d\mathbf{W}_i^{**}}{dt} + \frac{\mathcal{F}_{i+\frac{1}{2}}^{**} - \mathcal{F}_{i-\frac{1}{2}}^{**}}{\Delta x} &= \mathcal{Q}(\mathbf{W}_i^{**}), \qquad t \in (t_n, t_{n+1}], \\ \mathbf{W}_i^{**}(t_n) &= \mathbf{W}_i^*(t_n). \end{aligned} \tag{21}$$

Step 3:

$$\begin{aligned} \frac{d\mathbf{W}_i^{***}}{dt} &= \mathcal{S}(\mathbf{W}_i^{***}), \qquad t \in (t_n, t_{n+1}], \\ \mathbf{W}_i^{***}(t_n) &= \mathbf{W}_i^{**}(t_{n+1}). \end{aligned} \tag{22}$$

Note that in (21), the numerical fluxes are defined by $\mathcal{F}_{i\pm\frac{1}{2}}^{**} = \mathbf{F}(\mathbf{W}_{i\pm\frac{1}{2}}^{**})$. To complete the above time integration, the explicit third-order Runge-Kutta scheme investigated in [35] is used for the three steps (20)-(22). Hence, to advance the solution of an ordinary differential equation of the form (20), the Runge-Kutta scheme is carried out as

$$\begin{aligned} \mathcal{W}_i^{(1)} &= \mathbf{W}_i^n + \Delta t_n \mathcal{R}(\mathbf{W}_i^n), \\ \mathcal{W}_i^{(2)} &= \frac{3}{4}\mathbf{W}_i^n + \frac{1}{4}\mathcal{W}_i^{(1)} + \frac{1}{4}\Delta t_n \mathcal{R}(\mathcal{W}_i^{(1)}), \\ \mathbf{W}_i^{n+1} &= \frac{1}{3}\mathbf{W}_i^n + \frac{2}{3}\mathcal{W}_i^{(2)} + \frac{2}{3}\Delta t_n \mathcal{R}(\mathcal{W}_i^{(2)}), \end{aligned} \tag{23}$$

where we have dropped the asterisk from the variables in (20) for ease of the notation. It should also be stressed that the Runge-Kutta method (23) is a convex combination of first-order Euler steps which exhibits strong stability properties and it has been widely used for time integration of hyperbolic systems of conservation laws. It is also clear that using the time stepping scheme (23), no nonlinear or linear systems of algebraic equations are needed to be solved. In addition, the scheme (23) is Total Variation Diminishing (TVD), third-order accurate in time and stable under the standard Courant-Friedrichs-Lewy (CFL) condition

$$\Delta t_n \leq \frac{\Delta x}{\max\limits_i \left(\left|\lambda_{1,i}^n\right|, \left|\lambda_{2,i}^n\right|, \left|\lambda_{3,i}^n\right|, \left|\lambda_{4,i}^n\right| \right)}, \tag{24}$$

where $\lambda_{k,i}^n$ ($k = 1, 2, 3, 4$) are the eigenvalues defined in (29). It should be noted that as the spatial discretization is second-order accurate in the present work, a second-order time integration scheme would be enough to guarantee an overall second-order accuracy of the method. However, the third-order time stepping (23) is used here mainly to allow larger time steps to be used in the simulations. Notice that numerical simulations have also been performed using an explicit second-order Runge-Kutta scheme and the considered third-order scheme but not reported here for brevity, and we have observed no improvements in the overall accuracy of the approach but the third-order scheme can use time steps almost ten times larger than those used in its second-order counterpart for the same accuracy. It is also worth noting that (24) is a necessary condition for the stability of any explicit time integration scheme used for solving hyperbolic systems of conservation laws as (13). However, the stability region defined by the inequality (24) differs from one method to another and the third-order scheme used in the current study belongs to a class of Strong Stability Preserving (SSP) Runge-Kutta methods and it has been proven to have a larger stability region compared to its second-order counterpart, see [36] for further discussions on SSP methods.

To finalize the spatial discretization (19), a numerical reconstruction of the fluxes $\mathcal{F}_{i\pm\frac{1}{2}}^n$ and approximations of source terms $\mathcal{Q}(\mathbf{W}_i)$, $\mathcal{R}(\mathbf{W}_i)$ and $\mathcal{S}(\mathbf{W}_i)$ are required. In practice, this step can be achieved using any finite volume

method developed in the literature for solving a hyperbolic system of conservation laws with source terms. In the current study, we use a second-order finite volume method using limiters between Roe and Lax-Wendroff fluxes as discussed in [29]. Notice that flux limiters can be applied using either the characteristic variables or the physical variables in the hyperbolic systems of conservation laws. In our approach, we used the later reconstruction for its simplicity and no differences have been detected in the results obtained using both reconstructions for the considered examples. Discussions on the used flux-limiter method for sediment transport problems can be found in [29] and they are omitted here. Hence, the numerical fluxes $\mathcal{F}_{i+\frac{1}{2}}$ in (19) are computed as

$$\mathcal{F}_{i+\frac{1}{2}} = \phi_{i+\frac{1}{2}} \mathcal{F}^{LW}_{i+\frac{1}{2}} + \left(1 - \phi_{i+\frac{1}{2}}\right) \mathcal{F}^{Roe}_{i+\frac{1}{2}}, \tag{25}$$

with $\mathcal{F}^{Roe}_{i+\frac{1}{2}}$ is the numerical flux obtained using the Roe scheme as

$$\mathcal{F}^{Roe}_{i+\frac{1}{2}} = \frac{1}{2}\Big(\mathbf{F}(\mathbf{W}_{i+1}) + \mathbf{F}(\mathbf{W}_i)\Big) - \frac{1}{2}\,|\mathbf{A}|\left(\widehat{\mathbf{W}}_{i+\frac{1}{2}}\right)(\mathbf{W}_{i+1} - \mathbf{W}_i)\,, \tag{26}$$

where the averaged state $\widehat{\mathbf{W}}_{i+\frac{1}{2}}$ is calculated as

$$\widehat{\mathbf{W}}_{i+\frac{1}{2}} = \begin{pmatrix} \dfrac{h_i + h_{i+1}}{2} \\ \dfrac{\sqrt{h_i}\, v_i + \sqrt{h_{i+1}}\, v_{i+1}}{\sqrt{h_i} + \sqrt{h_{i+1}}} \\ \dfrac{\sqrt{h_i}\, c_i + \sqrt{h_{i+1}}\, c_{i+1}}{\sqrt{h_i} + \sqrt{h_{i+1}}} \\ \dfrac{Z_i + Z_{i+1}}{2} \end{pmatrix}, \tag{27}$$

and the Roe matrix in (26) is defined as $\mathbf{A} = \mathbf{R}|\mathbf{\Lambda}|\mathbf{R}^{-1}$ with

$$\mathbf{R} = \begin{pmatrix} -g\widehat{h} & \dfrac{\rho_s - \rho_w}{2\rho} & 1 & 1 \\ 0 & \dfrac{\rho_s - \rho_w}{2\rho}\widehat{v} & \widehat{\lambda}_3 & \widehat{\lambda}_4 \\ -g\widehat{h}\widehat{c} & \dfrac{\rho_s - \rho_w}{2\rho}\widehat{c} - 1 & \widehat{c} & \widehat{c} \\ g\widehat{h} - \widehat{v}^2 & 0 & 0 & 0 \end{pmatrix}, \qquad \mathbf{\Lambda} = \begin{pmatrix} \widehat{\lambda}_1 & 0 & 0 & 0 \\ 0 & \widehat{\lambda}_2 & 0 & 0 \\ 0 & 0 & \widehat{\lambda}_3 & 0 \\ 0 & 0 & 0 & \widehat{\lambda}_4 \end{pmatrix}, \tag{28}$$

with $\widehat{\lambda}_k$ ($k = 1, 2, 3, 4$) are the four eigenvalues associated with the system (13) and given by

$$\widehat{\lambda}_1 = 0, \qquad \widehat{\lambda}_2 = \widehat{v}, \qquad \widehat{\lambda}_3 = \widehat{v} - \sqrt{g\widehat{h}}, \qquad \widehat{\lambda}_4 = \widehat{v} + \sqrt{g\widehat{h}}. \tag{29}$$

where $\widehat{h}, \widehat{v}$ and $\widehat{c}$ are water height, water velocity and sediment concentration calculated at the averaged state given in (27). On the other hand, the numerical flux $\mathcal{F}^{LW}_{i+\frac{1}{2}}$ is obtained using the Lax-Wendroff scheme as

$$\mathcal{F}^{LW}_{i+\frac{1}{2}} = \frac{1}{2}\left(\mathbf{F}(\mathbf{W}_{i+1}) + \mathbf{F}(\mathbf{W}_i)\right) - \frac{\Delta x}{2\Delta t}\mathbf{A}\left(\widehat{\mathbf{W}}_{i+\frac{1}{2}}\right)\left(\mathbf{F}(\mathbf{W}_{i+1}) - \mathbf{F}\left(\mathbf{W}_i\right)\right). \tag{30}$$

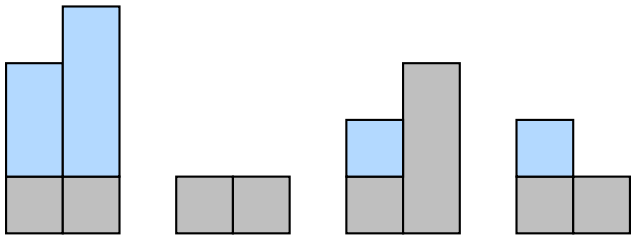

Figure 2: Illustration of the four possible wet/dry cells considered in the finite volume solution.

In (25), $\phi_{i+\frac{1}{2}} = \phi\left(r_{i+\frac{1}{2}}\right)$ is the limiter defined using an appropriate function ϕ of the ratio $r_{i+\frac{1}{2}}$ measuring the upwind to the local changes calculated locally for each component W of the vector $\mathbf{W}$ as

$$r_{i+\frac{1}{2}} = \frac{W_{i+1-q} - W_{i-q}}{W_{i+1} - W_i}, \qquad \text{with} \qquad q = \text{sgn}\left[\mathbf{\Lambda}_{i+\frac{1}{2}}\right].$$

As a flux limiter function we consider the well-known van Leer function

$$\phi(r) = \frac{|r| + r}{1 + |r|}. \tag{31}$$

Note that by setting $\phi = 0$ or $\phi = 1$, the reconstruction (25) yields the first-order Roe method or the second-order Lax-Wendroff method, respectively. In many applications in sediment transport, the Roe method would produce very diffusive numerical solutions due to the first-order accuracy and the Lax–Wendroff method would generate numerical oscillations due to the second-order accuracy. However, the flux-limited reconstruction (25) is a TVD method successfully capturing shocks and providing non-oscillatory solutions for the sediment transport equations. It is worth noting that the differential source term $\boldsymbol{Q}$ in (13) requires a careful numerical treatment such that discretizations of the flux gradients $\mathcal{F}_{i+\frac{1}{2}}$ and the source terms $\boldsymbol{Q}(\mathbf{W}_i)$ are well balanced in (19) following the concept of C-property reported in [29]. Hence, following similar formalism as in [29], the differential source terms $\boldsymbol{Q}(\mathbf{W}_i)$ are approximated in our method as

$$\boldsymbol{Q}(\mathbf{W}_i) = \begin{pmatrix} 0 \\ g\dfrac{h_{i+\frac{1}{2}} + h_{i-\frac{1}{2}}}{2}\dfrac{Z_{i+1} - Z_{i-1}}{2\Delta x} - \dfrac{(\rho_s - \rho_w)}{2\rho_i} g\left(\dfrac{h_{i+\frac{1}{2}} + h_{i-\frac{1}{2}}}{2}\right)^2 \dfrac{c_{i+1} - c_{i-1}}{2\Delta x} \\ 0 \\ 0 \end{pmatrix}. \tag{32}$$

It is evident that using the above approximation of the source term $\boldsymbol{Q}(\mathbf{W}_i)$ in the discretization (19), the considered finite volume method is well balanced and it satisfies the C-property.

Another challenging problem in the sediment transport is the treatment of dry areas within the computational domain. The proposed finite volume method should be able to evaluate the evolution of sediment transport at different changes in the water height including dry areas. In general, four cases may occur depending on the water availability in the two adjacent cells namely, (i) both cells contain the water with a depth higher than zero (two wet cells) which generate flux and momentum exchanges in these two cells, (ii) both cells are dry with water depths equal to zero, (iii) one cell is wet and the second one is dry but the elevation of the dry cell is higher than the wet cell, and (iv) the water height in the wet cell is higher than the elevation of the dry cell, see Figure 2 for an illustration of these four cases. Similar cases were also considered in [37] for solving shallow water flows over dry fixed beds. Note that the mass and momentum exchanges between the two considered cells are expected in the first and fourth cases and not in the second and third cases. Thus, to allow this in the finite volume method, a wet/dry treatment is carried out by adjusting

the water height as follows

$$h(t,x) = \begin{cases} h_i, & \text{if} \quad \eta_i > Z_{max}, \\ \dfrac{1}{2}\left(h_i + Z_i - Z_{min}\right), & \text{if} \quad \eta_i > Z_{min}, \\ \max\left(Z_{min} - Z_i, 0\right), & \text{if} \quad \eta_i < Z_{min}, \\ 0, & \text{otherwise}, \end{cases} \tag{33}$$

where $\eta_i = h_i + Z_i$ is the water free-surface, Z_{min} and Z_{max} are the minimum and maximum elevations defined as

$$Z_{min} = \min\left(Z_i, Z_{i+1}\right), \qquad Z_{max} = \max\left(Z_i, Z_{i+1}\right).$$

It is worth mentioning that using the wet/dry treatment (33) in the finite volume solution, the water height, water velocity and sediment concentration are set to zero in case of the two dry cells. It is also evident that the wet/dry treatment (33) guarantees the positivity of the finite volume method. On the other hand, for small water depths, the bed friction term τ_f becomes dominant compared to the other terms in the momentum equation in (1). This is mainly attributed to the definition of τ_f in (3) which contains the term $h^{\frac{1}{3}}$ in the denominator. In this study, to overcome this drawback a semi-implicit time integration of the source term $\mathcal{S}$ in (22) is implemented as

$$\begin{aligned} \frac{h^{n+1} - \widetilde{h}}{\Delta t_n} &= 0, \\ \frac{(hv)^{n+1} - \left(\widetilde{hv}\right)}{\Delta t_n} &= -gM_b^2 \frac{(hv)^{n+1}\,|\widetilde{v}|}{\left(\widetilde{h}\right)^{\frac{4}{3}}}, \end{aligned} \tag{34}$$

where $\widetilde{h}$ and $\widetilde{v}$ are respectively, the water height and water velocity obtained from the first step (21) of the splitting procedure. Solving for $(hv)^{n+1}$ the second equation in (34) results in

$$(hv)^{n+1} = \frac{\left(\widetilde{hv}\right)}{1 + \Delta t_n g M_b^2 \dfrac{|\widetilde{v}|}{\left(\widetilde{h}\right)^{\frac{4}{3}}}}. \tag{35}$$

Note that the wet/dry treatment (33) and the time integration of the friction term (35) are crucial for the numerical stability of the proposed finite volume method solving sediment transport problems particularly for dam-break flows over erodible dry beds.

3.2. Finite element solution of elasticity

In this section, a finite element method is used for solving the two-dimensional elasticity equations (15) using quadratic elements on unstructured triangular meshes. As in most finite element methods, the variational formulation of the strain energy in the spatial domain Ω is obtained by multiplying the first equation in (15) by a weight function ϕ_x and integrate over the domain as

$$\int_\Omega \frac{\partial \sigma_x}{\partial x}\phi_x \, d\mathbf{x} + \int_\Omega \frac{\partial \tau_{xz}}{\partial z}\phi_x \, d\mathbf{x} - \int_\Omega f_x \phi_x \, d\mathbf{x} = 0.$$

Using the well known Green-Gauss theorem, the above equation yields

$$\oint_{\partial\Omega} \sigma_x n_x \phi_x \, d\mathbf{x} - \int_\Omega \frac{\partial \phi_x}{\partial x}\sigma_x \, d\mathbf{x} + \oint_{\partial\Omega} \tau_{xz} n_z \phi_x \, d\mathbf{x} - \int_\Omega \frac{\partial \phi_x}{\partial z}\tau_{xz} \, d\mathbf{x} - \int_\Omega f_x \phi_x \, d\mathbf{x} = 0,$$

where $\mathbf{x} = (x,z)^\top$ and $\mathbf{n} = (n_x, n_z)^\top$ is the outward unit normal on $\partial\Omega$. Using the x-component of the traction $t_x = \sigma_x n_x + \tau_{xz} n_z$, the above equation can be reformulated as

$$\oint_{\partial\Omega} t_x \phi_x \, d\mathbf{x} - \int_\Omega \left(\frac{\partial \phi_x}{\partial x}\sigma_x + \frac{\partial \phi_x}{\partial z}\tau_{xz}\right) d\mathbf{x} - \int_\Omega f_x \phi_x \, d\mathbf{x} = 0. \tag{36}$$

Applying similar steps to the second equation in (15) gives

$$\oint_{\partial\Omega} t_z\phi_z \, d\mathbf{x} - \int_\Omega \left(\frac{\partial \phi_z}{\partial x}\tau_{xz} + \frac{\partial \phi_z}{\partial z}\sigma_z \right) d\mathbf{x} - \int_\Omega f_z\phi_z \, d\mathbf{x} = 0, \tag{37}$$

where $t_z = \sigma_z n_z + \tau_{xz} n_x$. By summing the two equations (36) and (37) we obtain

$$\oint_{\partial\Omega} (t_x\phi_x + t_z\phi_z) \, d\mathbf{x} - \int_\Omega (f_x\phi_x + f_z\phi_z) \, d\mathbf{x} - \int_\Omega \left(\frac{\partial \phi_x}{\partial x}\sigma_x + \frac{\partial \phi_x}{\partial z}\tau_{xz} + \frac{\partial \phi_z}{\partial z}\sigma_z + \frac{\partial \phi_z}{\partial x}\tau_{xz} \right) d\mathbf{x} = 0,$$

which can be rewritten in a compact vector form as

$$\int_\Omega \widehat{\boldsymbol{\phi}} \cdot \boldsymbol{\sigma} \, d\mathbf{x} = \oint_{\partial\Omega} \boldsymbol{\phi}^\top \cdot \boldsymbol{t} \, d\mathbf{x} + \int_\Omega \boldsymbol{\phi}^\top \cdot \boldsymbol{f} \, d\mathbf{x}, \tag{38}$$

where $\boldsymbol{\phi} = (\phi_x, \phi_z)^\top$, $\boldsymbol{t} = (t_x, t_z)^\top$, $\boldsymbol{f} = (f_x, f_z)^\top$ and $\widehat{\boldsymbol{\phi}} = \left(\frac{\partial \phi_x}{\partial x}, \frac{\partial \phi_z}{\partial z}, \frac{\partial \phi_x}{\partial z} + \frac{\partial \phi_z}{\partial x} \right)^\top$. For the finite element approximation of the weak form (38), we first discretize the spatial domain Ω into a set of triangular elements such that the approximated finite element solution is obtained in terms of the nodal values U_j and the polynomial basis functions $N_j(x, z)$ as

$$\mathbf{u}(x, z) = \sum_{j=1}^{N_d} \mathbf{U}_j N_j(x, z), \tag{39}$$

where N_d is the number of nodes in the computational mesh. Here, we implement quadratic triangular elements with six nodes for which the element displacement $\mathbf{u}^e = (u_x^e, u_z^e)^\top$ is obtained by

$$\mathbf{u}^e = \begin{pmatrix} N_1^e & 0 & N_2^e & 0 & \dots & 0 \\ 0 & N_1^e & 0 & N_2^e & \dots & N_6^e \end{pmatrix} \begin{pmatrix} u_{x1} \\ u_{z1} \\ u_{x2} \\ u_{z2} \\ \vdots \\ u_{x6} \\ u_{z6} \end{pmatrix},$$

where N_j^e are the shape functions expressed in the local coordinates $(\xi_1, \xi_2)^\top$ as

$$N_1^e(\xi_1, \xi_2) = \xi_2 \, (2\xi_2 - 1) \, , \qquad N_2^e(\xi_1, \xi_2) = \xi_1 \, (2\xi_1 - 1) \, ,$$

$$N_3^e(\xi_1, \xi_2) = (1 - \xi_1 - \xi_2) \, (1 - 2\xi_1 - 2\xi_2) \, , \qquad N_4^e(\xi_1, \xi_2) = 4\xi_2\xi_1 ,$$

$$N_5^e(\xi_1, \xi_2) = 4\xi_1 \, (1 - \xi_2 - \xi_1) \, , \qquad N_6^e(\xi_1, \xi_2) = 4 \, (1 - \xi_2 - \xi_1) \, \xi_2 .$$

Hence, once the elementary matrices are built and assembled into a global system of equations, the finite element solution is obtained by solving a linear system of algebraic equations as

$$[\mathbf{K}] \, \{\mathbf{u}\} = \{\boldsymbol{f}\} \, , \tag{40}$$

where $[\mathbf{K}]$ is the global stiffness matrix, $\{\mathbf{u}\}$ the nodal displacement vector and $\{\boldsymbol{f}\}$ the force vector. It should be stressed that we have used the constitutive stress-strain relation (17) to reconstruct the linear system (40) which is solved for the displacement. In all our computations carried out in this study, the linear system (40) is solved using the conjugate gradient algorithm with an incomplete Cholesky decomposition and a stopping criteria set to 10^{-8} which is considered to be small enough to guarantee that the overall numerical errors are dominated by the method truncation errors.

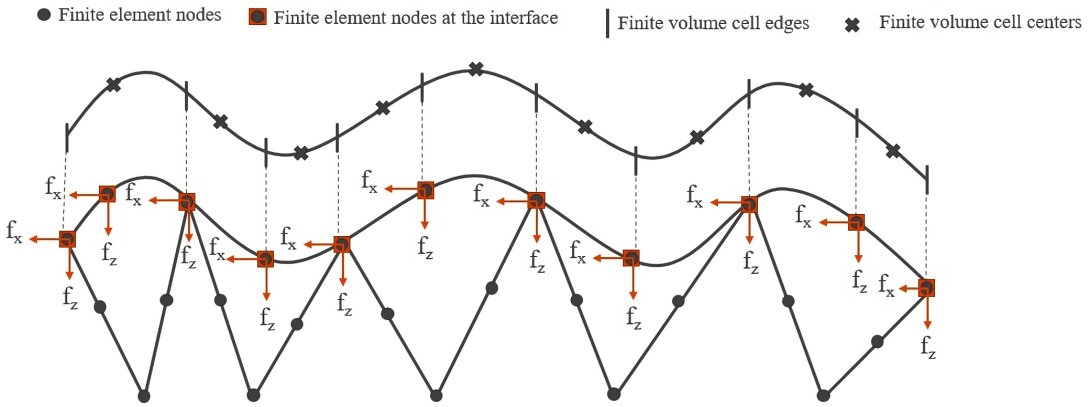

Figure 3: Illustration of finite element and finite volume nodes at the interface and distribution of the horizontal and vertical forces on the finite element nodes.

3.3. Transfer conditions at the bed-water interface

For the proposed model, coupling conditions are required to be transferred on the interface Γ at each time step between both sediment transport and elasticity models. As illustrated in Figure 3, the finite element and finite volume nodes on the interface do not in general coincide and therefore we employ a cubic spline interpolation to interchange the solutions between the two classes of nodes. Here, at each time step, the finite volume solutions of the sediment transport model are used to calculate the hydrostatic pressure and the friction distributions. These are then used to sample the horizontal and vertical forces at the interface to be used in the finite element solutions of the elasticity model. Thus, the horizontal force f_x in the x-direction is calculated using the friction term as

$$f_x = -g\tau_f^{n+1}. \tag{41}$$

Similarly, the vertical force f_z in the z-direction is computed at each time step using the variation in the hydrostatic pressure as

$$P^{n+1} = -\rho_0 g \frac{h^{n+1} - h^n}{\Delta t_n}. \tag{42}$$

Therefore, for each node of the three finite element nodes located on the interface Γ, the vertical force f_z is reconstructed using the integral form as [38]

$$\begin{aligned} f_z^{(1)} &= \int_{-1}^{1} -\frac{1}{2}\xi(1-\xi)\,P^{n+1}\frac{\hbar}{2}\,d\xi \;\approx\; \frac{\hbar}{6}P^{n+1}, \\ f_z^{(2)} &= \int_{-1}^{1} \left(1-\xi^2\right)P^{n+1}\frac{\hbar}{2}\,d\xi \;\approx\; \frac{2\hbar}{3}P^{n+1}, \\ f_z^{(3)} &= \int_{-1}^{1} \frac{1}{2}\xi(1+\xi)\,P^{n+1}\frac{\hbar}{2}\,d\xi \;\approx\; \frac{\hbar}{6}P^{n+1}, \end{aligned} \tag{43}$$

where $\hbar$ is the length of the edge in the considered triangular element on the interface. Hence, once the element forces $f_z^{(1)}$, $f_z^{(2)}$ and $f_z^{(3)}$ are calculated according to (43), the global force f_z to be applied in the z-direction is calculated by accumulating the elemental forces on the overlapped nodes as illustrated in Figure 3. Note that it is easy to verify that the element forces (43) satisfy the relation

$$f_z^{(1)} + f_z^{(2)} + f_z^{(3)} = \hbar P^{n+1}.$$

Algorithm 1 Hybrid finite element/finite volume for stress fields induced by shallow water flows on movable beds.

Require: E, ν, p, ρ_w, ρ_s, M_b, θ_c, T, C_r.

while $t_n \leqslant T$ **do**
  Solve the shallow water equations using:
  for each control volume $\left[x_i, x_{i+\frac{1}{2}}\right]$ **do**
    Compute the flux limiter numerical fluxes $\mathbf{F}^n_{i+\frac{1}{2}}$, following the equations (25)-(30).
    Discrete the source term $\mathbf{Q}_i$ using the well-balanced discretization (32).
    Compute the solution in the first stage of the splitting $\mathbf{W}_i^{n+1}$ using (21).
    Compute the solution in the second and third stages of the splitting $\mathbf{W}_i^{n+1}$ using (21) and (22).
  end for
  Compute the horizontal force f_x using the bed friction according to (41).
  Compute the vertical force f_z using the hydrostatic pressure according to (42).
  Assemble the stiffness matrix $\mathbf{K}$ for the elastostatic system using the finite element method (36)-(40).
  Assemble the force vector $\boldsymbol{f}$ for the elastostatic system using the finite element method (36)-(40).
  Update the linear system (40) for the displacement in the computational mesh.
  Update the linear system (16) for the elastic strain in the computational mesh.
  Update the linear system (17) for the stresses distributions in the computational mesh.
  Update the displacement of the finite element nodes on the interface.
  Update the time step Δt according to the CFL condition (44).
  Overwrite $t_n \longleftarrow t_n + \Delta t$ and go to step 2.
end while

In addition, since both the horizontal force f_x and vertical force f_z have negative signs, these forces are applied in the negative x- and z-direction, respectively. In summary and for completeness, the coupled finite volume/finite element method proposed in the present study for the stresses induced by shallow water flows on movable beds is carried out in the steps described in Algorithm 1. It should be stressed that the system is fully coupled for which the coupling conditions occur on the interface Γ between the two models. Here, given the computational domain Ω and the sediment transport solutions at time $t = t_n$, the sediment transport equations (13) are solved to obtain the water depth h, the water velocity v, the sediment concentration c and the bed profile Z at next time $t = t_{n+1}$. Then, these sediment variables are employed to calculate the horizontal and vertical forces f_x and f_z using the equations (41) and (43), respectively. Next, these forces are imposed on the interface Γ to solve the elasticity equations (15)-(17) on the original domain Ω at time $t = t_n$ to obtain the stress distributions in the bed. Therefore, the sediment transport influences the stress distributions and the bed deformation influences the water flow as well. Notice that the coupling between the two models occurs through the boundary conditions applied to the bed-surface in the linear elasticity model by applying the friction force computed in the shallow water model. Thus, the bed shear-stress τ_f computed from Manning law is applied as a boundary condition for the elastic model. More precisely, the friction force τ_f is interpreted as the tangential stress on the bed-surface and it acts as an external load in the finite element analysis. Hence, the force $f_x = -g\tau_f$ is used in the elasticity model (15) which is applied to the surface of the bed as a traction boundary condition.

4. Numerical results and examples

To assess the performance of the proposed numerical models and computational methods we present results for well-established problems for shallow water flows on movable beds and resolve distributions of the induced stress fields. We also verify the numerical capability of these techniques to solve moving wet/dry fronts in shallow water flows. In all our simulations presented in this section, the Courant number is fixed to $C_r = 0.75$ and the time step Δt_n is dynamically adjusted at each time step according to the CFL stability condition (24) as

$$\Delta t_n = \mathrm{Cr}\frac{\Delta x}{\max\left(\left|\lambda_1^n\right|, \left|\lambda_2^n\right|, \left|\lambda_3^n\right|, \left|\lambda_4^n\right|\right)}, \tag{44}$$

Table 1: Reference parameters used in our simulations.

Quantity	Reference value	Quantity	Reference value
E	10000 MPa	ν	0.3
g	9.81 m/s^2	M_b	0.025 $s/m^{1/3}$
ρ_w	1000 kg/m^3	μ	1.2×10^{-3} Ns/m^2
p	0.67	θ_c	0.0145

where λ_1, λ_2, λ_3 and λ_4 are the four eigenvalues of the shallow water equations defined in (29). In all the computations reported in this study unless mentioned otherwise, the selected values for the evaluation of the present techniques are summarized in Table 1.

4.1. Verification of the well-balanced property

We first demonstrate that the proposed method preserves the correct steady-state solution and satisfies the well-balanced property by considering a test problem similar to the examples investigated in [39]. Thus, the channel is 1000 m long subject to the following initial conditions

$$h(0,x) = 10\ m - Z(0,x), \quad v(0,x) = 0\ m/s, \quad \text{and} \quad c(0,x) = 0,$$

with the initial bed is defined as

$$Z(0,x) = \begin{cases} \sin^2\left(\dfrac{(x-300)\pi}{200}\right), & \text{if } 300 \le x \le 500; \\ 0, & \text{elsewhere.} \end{cases} \tag{45}$$

For this problem, we set $\mathcal{E} - \mathcal{D} = 0$, $\rho_s = 1650\ kg/m^3$, $M_b = 0$ and we display the results at the final time $t = 238000\ s$ using 100 control volumes for the spatial discretization. In Figure 4, we present the water free-surface for this test problem along with the errors calculated as differences between the simulated water free-surface and its exact value of 10 m. It is clear from these results that the water free-surface remains constant during the simulation times indicating that the proposed method preserves the well-balanced property to the machine precision. This confirms that the numerical scheme accurately maintains a balance between the flux gradients and the source terms, ensuring that a still water surface remains unchanged throughout the simulation. This demonstrates the effectiveness of our numerical method in preserving the well-balanced property, ensuring that the water free-surface does not deviate from its initial state when it should theoretically remain constant. Note that this verification is crucial for ensuring the reliability of the model in practical applications, where maintaining the correct water level over complex topography is essential.

4.2. Validation of the finite volume method solving shallow water flows on movable beds

To validate the well-balanced finite volume method used in the present study for shallow water flows on movable beds, we compare the numerical simulations and experimental measurements for a dam-break problem over a dry erodible bed. The experimental work was carried out at the university catholique de Louvain [40] and the same setup is adopted in our simulations. In this experiment, the channel is 2.5 m long, 10 cm wide and a sidewall height of 35 cm is used. The sediment bed is composed of cylindrical PVC pellets with a fixed diameter of 3.2 mm and height of 2.8 mm which is equivalent to a spherical diameter of 3.5 mm. For this problem, the sediment particle size $d_s = 1.72\ mm$, the sediment density $\rho_s = 2630\ kg/m^3$, the porosity $p = 0.39$ the erorion term $\mathcal{E}$ and deposition term $\mathcal{D}$ are respectively defined in (9) and (6) with constant coefficients $m = 2$ and $\varphi = 0.015$. At the upstream, the water level is raised to a depth of $h_0 = 10\ cm$ above the bed bottom. The sluice gate is then quickly lifted using weight to release the dam-break wave and pulley mechanism and the gate is verified to clear the water surface within 50 ms. The generated flow patterns are filmed through the transparent sidewalls using fast CCD cameras operating at 200 frames per second. For this experimental setup, two synchronized CCD cameras were available and the image sequences resulting from separate runs are collected to produce profiles of the free-surface and bed. These measurements for the

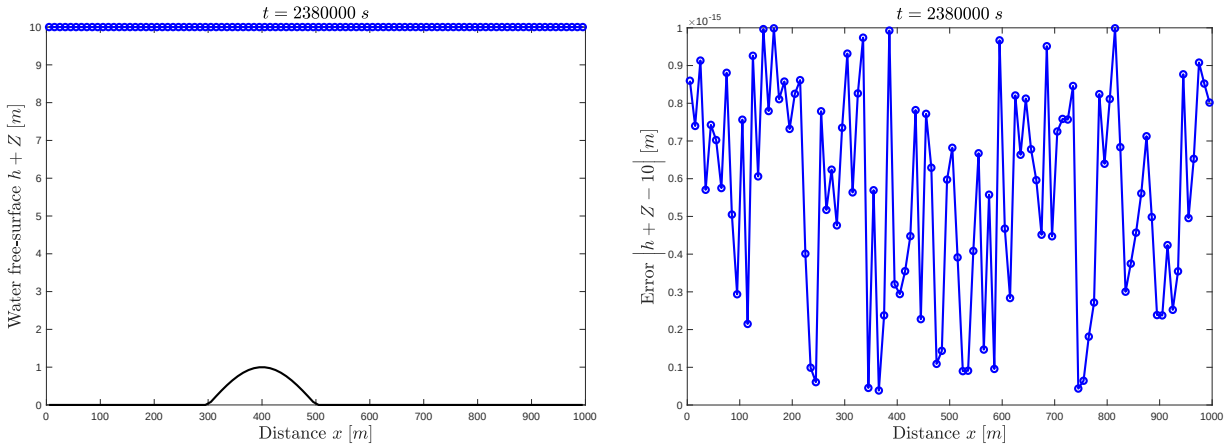

Figure 4: Water free-surface (left) and the coresponding errors (right) obtained using the well-balanced finite volume method solving a steady problem over a non-flat bed at time $t = 238000\ s$.

bed and water free-surface profiles are recorded at three different times $t = 5t_0$, $7.5t_0$ and $10t_0$, with $t_0 = \sqrt{\frac{h_0}{g}}$ is the hydrodynamic time scale and h_0 being the initial upstream depth of water. For the numerical simulations, we solve the sediment transport equations (13) equipped with the following initial conditions

$$Z(0,x) = 0\ m, \qquad h(0,x) = \begin{cases} 0.1\ m, & \text{if} \quad x \leq 1.25\ m, \\ 0\ m, & \text{if} \quad x > 1.25\ m, \end{cases} \qquad v(0,x) = 0\ m/s, \qquad c(0,x) = 0. \tag{46}$$

The comparison between the numerical results and experimental data at the three considered times is depicted in Figure 5. Here, a mesh with 200 control volumes is used in the simulations and profiles for the bed and water free-surface are included in this figure. As expected, at initial time $t = 0\ s$, the dam collapses and the hydraulic problem consists of a shock wave traveling downstream and a rarefaction wave traveling upstream. It can clearly be observed from these results that the erosion effects on the bed are accurately captured and a good agreement between the numerical results and the experimental data are obtained. For further validations for this problem, a comparison between the sediment concentration obtained using the proposed well-balanced finite volume method and the corresponding numerical results reported in [41] is presented in Figure 6 at $t = 0.25\ s$ and $t = 1\ s$. The computed results illustrate similar trends for the sediment concentration at both times with less numerical diffusion in the proposed well-balanced finite volume method compared to those results in [41]. Apparently, the overall features of water flow and sediments for this erosional dam-break problem are accurately resolved using the well-balanced finite volume method with no spurious oscillations appearing in the numerical results. Obviously, the computed results verify the stability and the shock capturing properties of the proposed finite volume method while the wet/dry treatment performs well for dam-break problems over dry beds with no need for heavily refined meshes.

4.3. Validation of the finite element method solving linear elasticity

To validate the unstructured finite element method, we consider the benchmark problem of linear elasticity studied in [10]. Here, the experimental study involves the measurement of vertical stress that occurs due to loading of a footing plate located on sand, along the centerline of a square footing at various depths of the sandy soil. The model tests were performed using a square shape box having dimensions of $B \times B \times B$ with $B = 70\ cm$ in the geotechnical laboratory of the civil engineering department at the Cukurova University. The sides of the box were reinforced by steel profiles to increase stiffness and two sides of the box consist of 8 *mm* thick glass plates and the other two sides are made of 20 *mm* thick wooden plates. In this experiment, the sand bed was prepared with a uniform relative density of approximately $D_r = 65\%$ and with the corresponding unit weight $\gamma = 17.1\ kN/m^3$. For this purpose, the glass plates of the test box

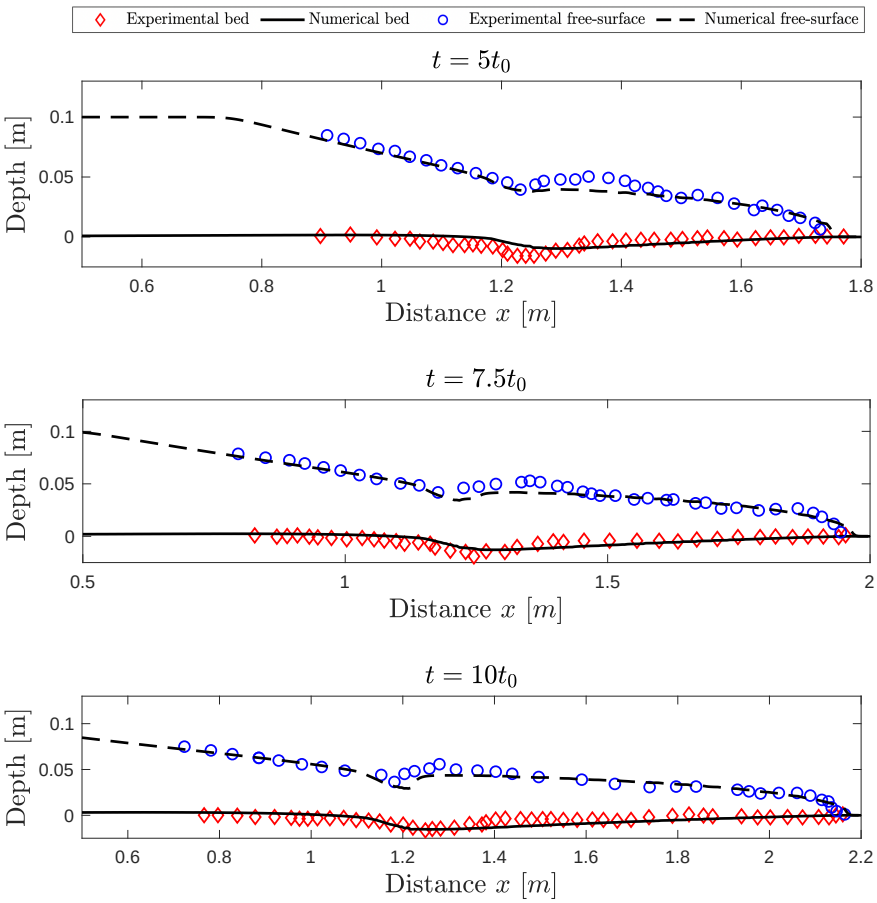

Figure 5: Comparison between experimental results presented in [40] and numerical results obtained using the well-balanced finite volume method solving a dam-break problem over a dry erodible bed at three different instants.

were scaled and each sand layer was compacted by a hand-held vibratory compactor up to the predetermined depths. For calculating the vertical stresses in the soil, a static loading was applied to the centre of the model footing in the vertical direction. The loading system used in the tests consisted of a 45 KN capacity mechanical jack supported against the loading frame. A proving ring was used to measure the load values applied to the model plate. In this model, a plate foot square is used in the test with a width of $R = L = 150$ mm, thickness of 20 mm and a vertical stress of 47 kN/m^2 capacity were implemented at the center of the square model. The vertical stresses that occur during loading beneath the center of the square footings were measured using a 10 bar capacity, diaphragm type, vertically mounted pressure transducer. For the numerical simulations, we run the finite element analysis on a mesh of 3694 elements and 6711 nodes solving the linear elasticity model (15) using the Young's modulus $E = 28000$ kN/m^2 and the Poisson's ratio $\nu = 0.20$. A comparison between the obtained numerical, analytical and experimental vertical stresses at three different depths ($l/R = 1.0$ mm, $l/R = 1.5$ mm and $l/R = 2.0$ mm) are shown in Figure 7. Note that the Boussinesq analytical solution [42] is one of the most frequently used to solve the stress problem by a point load acting at the surface in a linearly elastic, homogeneous and isotropic space. According to this solution, the vertical stress value $\Delta\sigma_z$ due to a point load Q at any vertical depth l and at a point of horizontal distance of r is given as

$$\Delta\sigma_z(r,l) = \frac{3}{2\pi}\left(\frac{1}{1+\left(\frac{r}{l}\right)^2}\right)^{5/2}\frac{Q}{l}. \tag{47}$$

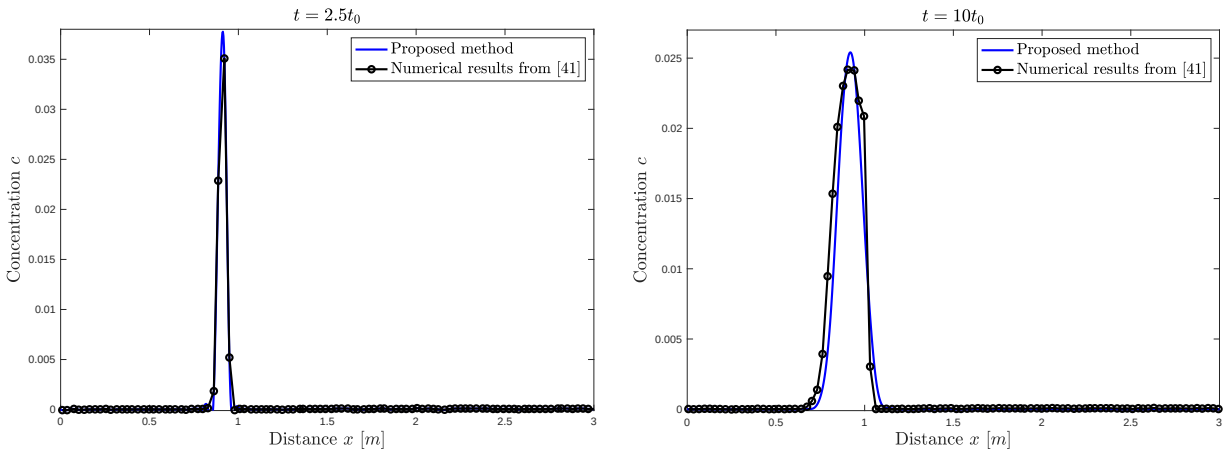

Figure 6: Numerical results for the sediment concentration obtained for the dam-break problem over a dry erodible bed at two different instants.

Table 2: Mesh statistics and obtained results for stresses induced by the dam-break problem over erodible bed at time $t = 1.7$ s. Here, the CPU times are given in seconds.

	# elements	# nodes	max (Z)	max (σ_z)	max (σ_x)	max (τ_{xz})	max $(\overline{\sigma})$	CPU time
Mesh A	901	1886	-1.219	267.768	872.9	963.3	2511.5	5.3
Mesh B	1819	3762	-1.469	355.637	1159.3	1279.4	3335.6	11.7
Mesh C	3624	6701	-1.619	566.483	17847.8	15747.8	3413.6	34.1
Mesh D	7248	14751	-1.669	833.158	19245.0	18251.3	3723.1	71.6
Reference	39591	80036	-1.673	837.891	19268.2	18284.3	3797.4	812.2

Since the point load affecting the soil surface is not realistic and most of the loads are uniformly distributed, the above equation can be reformulated to solve for the stresses induced from the distributed load as

$$\Delta\sigma_z(r,l) = \frac{q}{4\pi}\left(\frac{2RLl\left(R^2+L^2+2l^2\right)}{\left(R^2+l^2\right)\left(L^2+l^2\right)\sqrt{l^2+L^2+R^2}} + \tan^{-1}\left(\frac{2RLl\sqrt{l^2+L^2+R^2}}{-R^2L^2+l^2(R^2+L^2)+l^4}\right)\right), \tag{48}$$

where q is the uniformly distributed load. It can be seen from the comparison in Figure 7 that experimental results are in good agreement with numerical and theoretical results. In our simulations, the difference between the experimental results and those obtained using the finite element method and the analytical equations is about 6.5 % and 9.5 %, respectively. It should be noted for this example that the Boussinesq solution also gives smaller values than the numerical and experimental studies. However, our numerical results are more improved than the results presented in [10] as in our results, the experimental results are only 6.5 % greater than the results from our finite element model using a relatively coarser mesh than the one used in [10]. It should also be stressed that the difference between the experimental results and those reported in [10] is 14 %. This confirms the high accuracy of the proposed unstructured finite element method for solving stress fields.

4.4. Stresses induced by a dam-break problem over erodible bed

In this example, we investigate the stresses generated by a dam-break problem over erodible bed using the proposed coupled mode. In practice, these stresses are very important to be identified for different applications in soil mechanics and geotechnics. For instance, road cuts are one of the very critical applications of these stresses. It is very crucial to accurately identify the mass of soil that should be around, the rate of erodible and deposition soil,

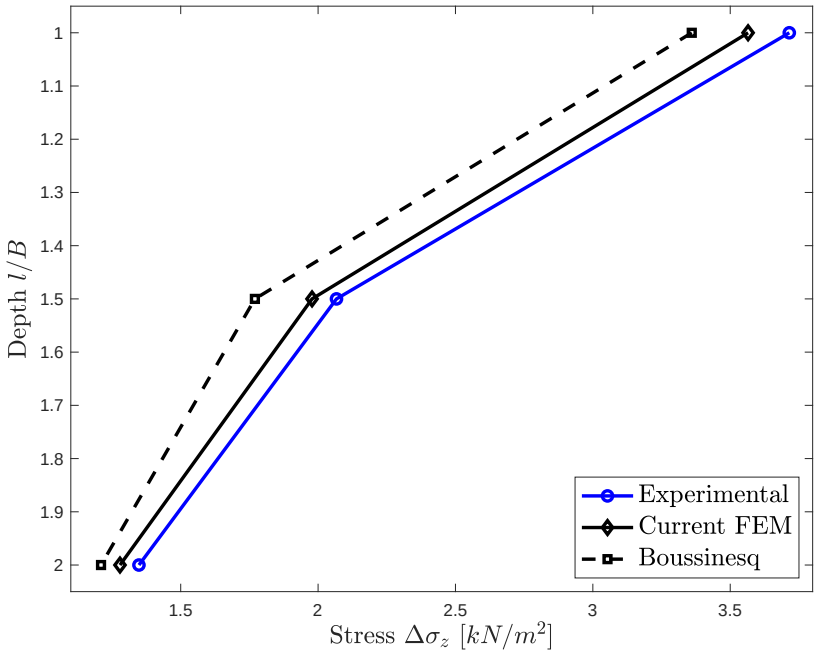

Figure 7: Comparison between experimental results presented in [10], theoretical and numerical results obtained using the unstructured finite element method solving stresses in a foot square domain.

the amounts and center of stresses induced in order to avoid any soil failure within the time. In our simulations, the computational domain is a channel 20 m long with a dam located at the center of the channel and characterized by the following initial conditions

$$Z(0,x) = 0, \qquad h(0,x) = \begin{cases} 2, & \text{if} \quad x \leq 0, \\ 0, & \text{if} \quad x > 0, \end{cases} \qquad v(0,x) = 0, \qquad c(0,x) = 0. \tag{49}$$

For this problem, the sediment particle size $d_s = 2.5\ mm$, the sediment density $\rho_s = 2650\ kg/m^3$, the erorion term $\mathcal{E}$ and deposition term $\mathcal{D}$ are respectively defined in (9) and (6) with coefficients m and φ defined in (8) and (10), respectively. The domain is discretized into 200 control volumes and at time $t = 0$ the dam breaks over the dry erodible bed resulting in a shock wave travelling downstream and upstream causing substantial erosion on the bed. The erosion effects are then passed to the bed through the interface leading to deformations in the bed. For this example, a depth of 7 m is accounted for the bed which results in a rectangular domain 20 m long and 7 m deep to be used for the stress analysis. To resolve the distribution of these stresses in the bed, we first perform a mesh convergence study. To this end, we consider four unstructured meshes with different element and node densities as shown in Figure 8. Notice that for accuracy reason, a denser mesh is used in the area where the erodibility occurs whereas a coarser mesh is used otherwise in the domain. To calculate reference solutions for this problem we also consider a very fine mesh in our simulations and it is not included in Figure 8 because of its density which results in a heavily black plot. In Table 2, we summarize the number of nodes and elements in each mesh along with the computational results obtained at the final time $t = 1.7\ s$ for the maximum deformation, maximum stresses and CPU times.

In Figure 9 we display the bed profiles obtained at time $t = 1.7\ s$ using the considered meshes. It is clear that large differences are detected between the results obtained using the coarse meshes Mesh A and Mesh B and results obtained using the reference mesh. Increasing the density of elements in the meshes, Mesh C and Mesh D generate similar bed profiles and the difference in results obtained on Mesh D and reference mesh becomes negligible. This is also confirmed by the results listed in Table 2 for the maximum deformation $\max(Z)$ and maximum stresses

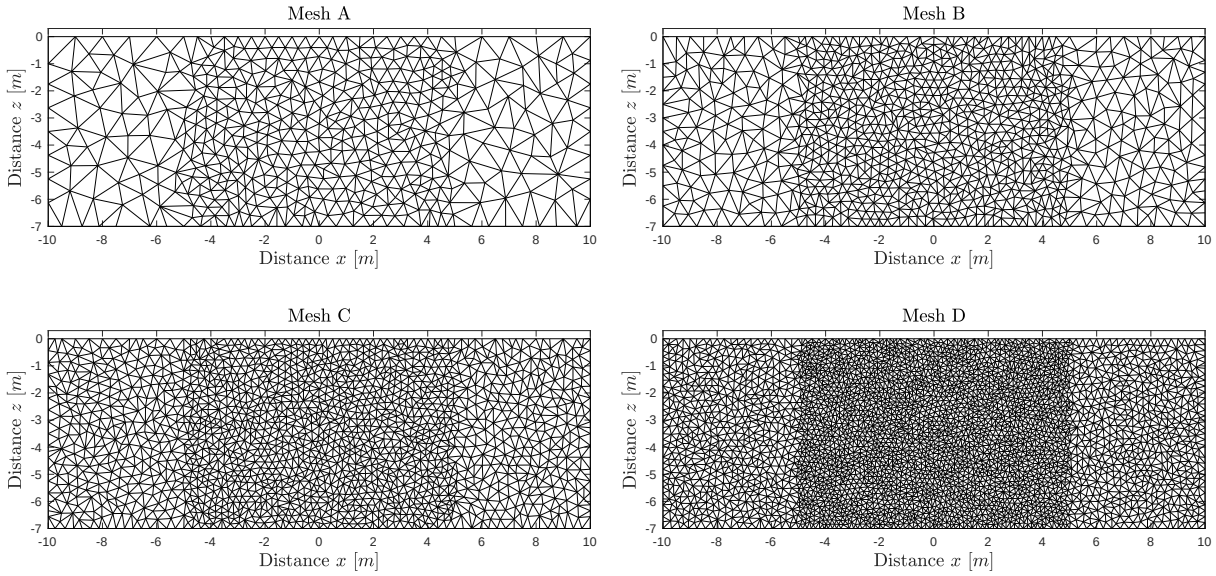

Figure 8: Meshes used in the simulation of stresses induced by the dam-break problem over erodible bed.

$\max(\sigma_z)$, $\max(\sigma_x)$, $\max(\tau_{xz})$ and $\max(\overline{\sigma})$. Needless to mention that, refining the mesh results in an increase in the computational cost, compare the CPU times for each mesh in Table 2. Therefore, Mesh D is used in the rest of our simulations as it compromises between the accuracy and the computational cost required to solve the stress fields for this dam-break problem over a movable bed. The main objective of this example is to investigate the stress distributions in bed resultant from the erosion by dam-break flow. It should be stressed that in all of the previous research on dam-break problems, the only measurable stress is the surface shear stress which does not give clear information about the stress distribution inside the overall bed topography.

Figure 10 depicts the field patterns obtained for the two normal stresses σ_x and σ_z, the shear stress τ_{xz} and the well known deviatoric stress $\overline{\sigma}$. As expected, high stress distributions are generated in the area where erosion takes place and then distributed horizontally and vertically throughout the bed. Note that the region where stresses are distributed can give a clear idea of the location of the high and low stresses, which gives an indication of the safety of these areas with regards to possibilities of the bed failure for different sediment transport scenarios. It is also clear that the deformed bed has been accurately resolved using the unstructured finite element method. For example, the symmetry of these stress distributions can also be clearly seen in Figure 10 and these stresses are correctly and accurately captured for this sediment transport problem. It should be stressed that results from the proposed coupled model should be compared with observations of laboratory free-surface flows and bed deformations for this problem. However, there is no data available until now to carry out this comparison study. Thus, at the moment we can only perform numerical simulations and verify that results are plausible and consistent for both hydraulic and stress solutions.

For further investigations of the stress distributions in the bed and their evolution within time, vertical cross-sections at the center of the domain $x = 0$ for the two main normal stresses σ_x and σ_z are illustrated in Figure 11. It can be clearly shown from the results in this figure that the stress magnitudes increase as the time evolves. It is also clear that the maximum horizontal and vertical stresses are detected at the final time $t = 1.1\ s$ when the erosion is the highest. However, both stresses are minimal at the beginning of simulations where the erosion reaches its minimum values. On the other hand, it can be clearly noted that the vertical stress attends higher values than its horizontal counterpart which is consistent with the direction of erosion in this test example. To assess the accuracy of the coupled model in dealing with the induced underground stresses, Figure 12 illustrates the time evolution of the shear and deviatoric stresses at three different points A_1, A_2 and A_3 located in the computational domain with coordinates $(0, -3)$, $(0, -4)$ and $(0, -5)$, respectively. Obviously, because of the symmetry in this problem, the deviatoric stress

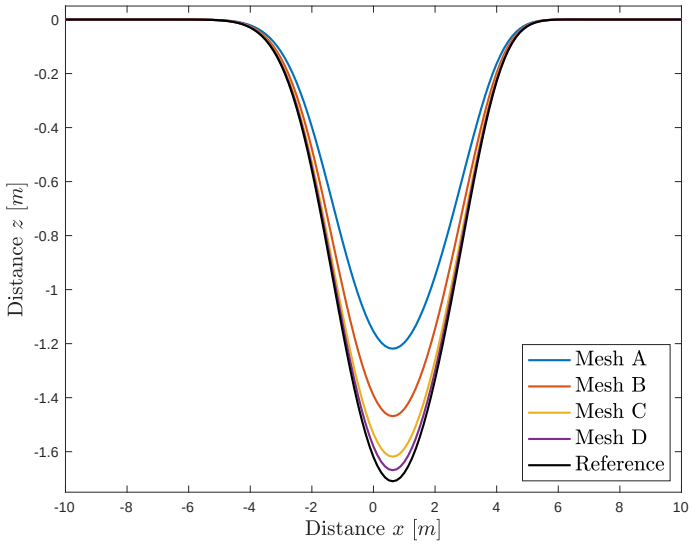

Figure 9: Comparison of bed profiles obtained for the problem of stresses induced by the dam-break problem over erodible bed using different meshes at time $t = 1.7\ s$.

is the highest at the point A_1 and the lowest at the point A_3. As time progresses, the deviatoric stress increases since the erosion level becomes high. The opposite behaviour is noticed in the case of the shear stress, where the highest value is obtained at the point A_3 and the lowest value is at the point A_1 while it can also be observed that the shear stress is decreasing as the time increases. The proposed coupling model performs well for this dam-break problem over erodible bed as it accurately captures the induced stresses without the requirement of complicated computational techniques for representations of the erodible bed.

4.5. Stresses induced by a stream-flow problem over a trench

We consider in this test example a steady stream-flow over a trench to investigate the resultant stresses in the bed topography using the proposed hybrid finite volume/finite element method. We also use this example to verify the capability of the well-balanced finite volume method to predict bed evolution under the steady stream-flow conditions using experimental measurements conducted at the Delft hydraulics laboratory and published in [43]. Here, the trench is 30 m long and it has sides of $1V : 10H$ slopes located in the middle of the domain. Initially, the flow is at rest with the water height set to $h = 0.39\ m$ and a velocity of $v = 0.51\ m/s$ prescribed as the upstream boundary condition. The geometry of the trench and its initial conditions are depicted in Figure 13 for more clarifications. The erodible bed is composed of fine sand with diameter $d_s = 0.115\ mm$, density $\rho_s = 2650\ kg/m^3$ and porosity $p = 0.4$. According to the experimental work in [43], the Manning coefficient is set to $M_b = 0.016\ s/m^{1/3}$. For this problem, the erorion term $\mathcal{E}$ and deposition term $\mathcal{D}$ are respectively defined in (9) and (6) with constant coefficients $m = 2$ and $\varphi = 0.015$. In addition, to maintain the sediment equilibrium conditions in the upstream for which no scour or deposition occurs, a sand with the same composition is fed at a constant rate of $0.04\ kg/s/m$. Therein, the suspended load transport rate was estimated to be $0.03 \pm 0.006\ kg/s/m$ and the bedload transport rate of about $0.01\ kg/s/m$. In our simulations, the computational domain is discretized into 200 control volumes. To achieve the steady flow conditions, the simulation is performed in two stages. In the first stage, the numerical model is run to 900 s while the bed profile is maintained fixed. After 900 s in the second stage, the sand is fed and the bed evolution occurs. In Figure 14, the obtained numerical results for the bed profile at time $t = 7.5\ hr$ and $t = 15\ hr$ are compared to the experimental measurements. A good agreement between the computational and experimental bed profiles can clearly be seen at the considered instants. Both erosion and deposition effects have been numerically resolved using the proposed approach without introducing non-physical oscillations or excessive numerical diffusion. Furthermore, the obtained results for the water free-surface profile in Figure 14 also confirm the well-balanced characteristic of the finite volume method as this profile remains flat at all times of the simulation.

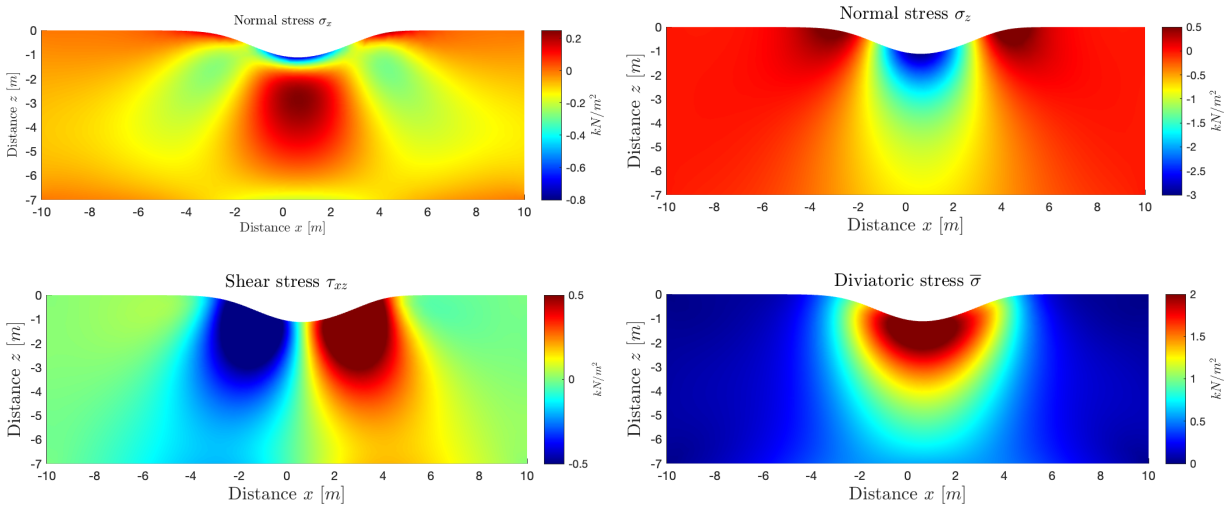

Figure 10: Snapshots of normal stresses σ_x and σ_z, shear stress τ_{xz} and deviatoric stress $\overline{\sigma}$ for the problem of stresses induced by the dam-break problem over erodible bed at time $t = 1.7\ s$.

Table 3: Mesh statistics and obtained results for stresses induced by the stream-flow problem over a trench at time $t = 7.5\ hrs$. The CPU times are given in minutes.

	# elements	# nodes	max (Z)	max (σ_z)	max (σ_x)	max (τ_{xz})	max $(\overline{\sigma})$	CPU time
Mesh A	942	1995	-0.1365	490.5	1647.4	985.5	2333.2	4.6
Mesh B	1882	3817	-0.1645	540.6	1815.6	1086.2	2571.4	9.8
Mesh C	3694	6711	-0.1813	557.3	1871.6	1119.8	2650.8	21.5
Mesh D	7406	15149	-0.1884	570.9	1917.6	1147.3	2715.9	51.1
Reference	39591	80036	-0.1912	581.4	1932.4	1189.3	2782.7	538.0

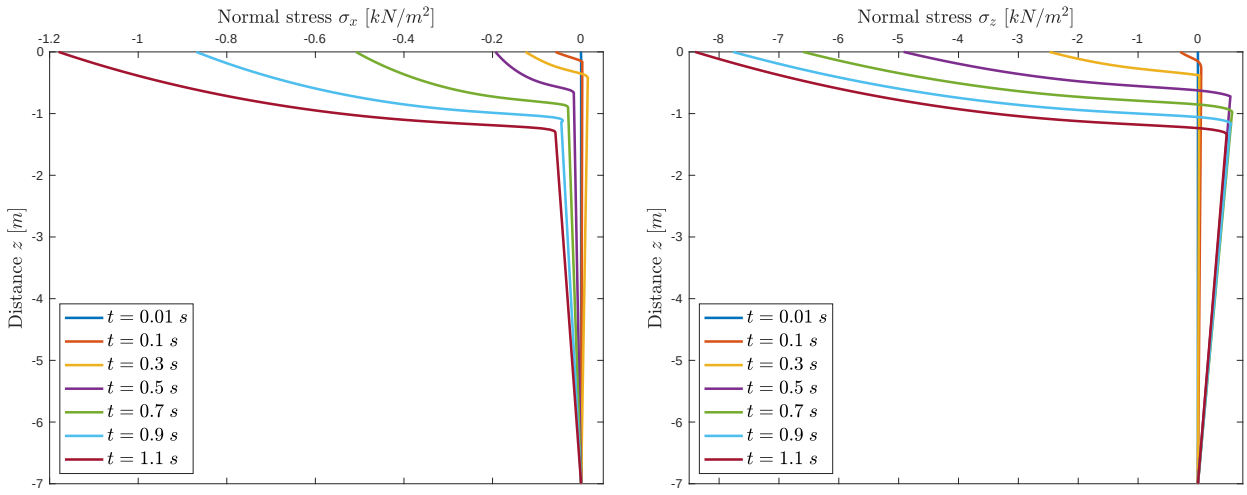

Figure 11: Vertical cross-sections of the normal stresses σ_x (left plot) and σ_z (right plot) obtained at different times for the problem of stresses induced by the dam-break problem over erodible bed.

As observed in the above simulations, the water flow causes erosion and deposition in the trench which are expected to transmit internal stresses in the bed. Therefore, we investigate the stresses induced by this stream-flow problem over the trench accounting for erosion and deposition effects. As in the previous example, we have also performed a mesh convergence study using the four unstructured meshes shown in Figure 15. Note that, to avoid refining the mesh everywhere in the computational domain, only the area subject to the deformation is refined in the mesh. Thus, this would require less computational cost than considering a uniformly fine mesh in the simulations. We also consider a very refined mesh as a reference for accuracy comparisons in this problem. In Table 3 we summarize the number of nodes and elements in each mesh along with the computational results obtained at final time $t = 7.5$ hr for the maximum deformation, maximum stresses and the CPU times. The bed profiles obtained at time $t = 7.5$ hr using the five considered meshes are depicted in Figure 16. As it can be seen from these results, the bed profile computed using the coarse meshes Mesh A and Mesh B are less accurate than the results obtained on the reference mesh. Refining the mesh, the results obtained using Mesh C and Mesh D appear similar and the difference in results obtained on Mesh D and reference mesh becomes negligible. These observations are also supported by the results presented in Table 3 for the maximum deformation max (Z) and maximum stresses max (σ_z), max (σ_x), max (τ_{xz}) and max $(\overline{\sigma})$. Regarding the computational cost for these simulations, the CPU time in Table 3 also reveals an increase in this cost as the mesh is refined. It can be clearly noted from these results that a mesh convergence is achieved in the unstructured finite element method as the bed deformation using Mesh D and the reference mesh is noticeably similar but with large differences in the computational cost. Based on these simulations, Mesh D is used in the rest of our computations as it compromises between the accuracy and the efficiency required to solve the stress fields for this stream-flow problem.

In Figure 17 we present the field patterns obtained for the two normal stresses σ_x and σ_z, the shear stress τ_{xz} and the deviatoric stress $\overline{\sigma}$ at time $t = 7.5$ hr. For a better insight, only a part of the computational domain is displayed in this figure. It is evident that the highest stresses are localized near areas with maximum deformations induced by erosion and deposition effects whereas low stresses are distributed elsewhere in the computational domain. The finite element method performs well in calculating the stresses in the bed and accurately capturing their effects due to erosion and deposition caused by the steady stream flow. Unlike the previous sediment transport problem for which only erosion occurred in the bed, in this problem both erosion and deposition take place and therefore the resultant stresses exhibit different patterns than those observed for the dam-break problem. To further investigate these stress distributions in the bed and their evolution within time, vertical cross-sections at the trench in $x = 16.5$ m for the two main normal stresses σ_x and σ_z are depicted in Figure 18. It is also noticeable from these results that the computed stresses increase as the time progresses which results in more deposition in the trench. At the final time $t = 7.5$ hr,

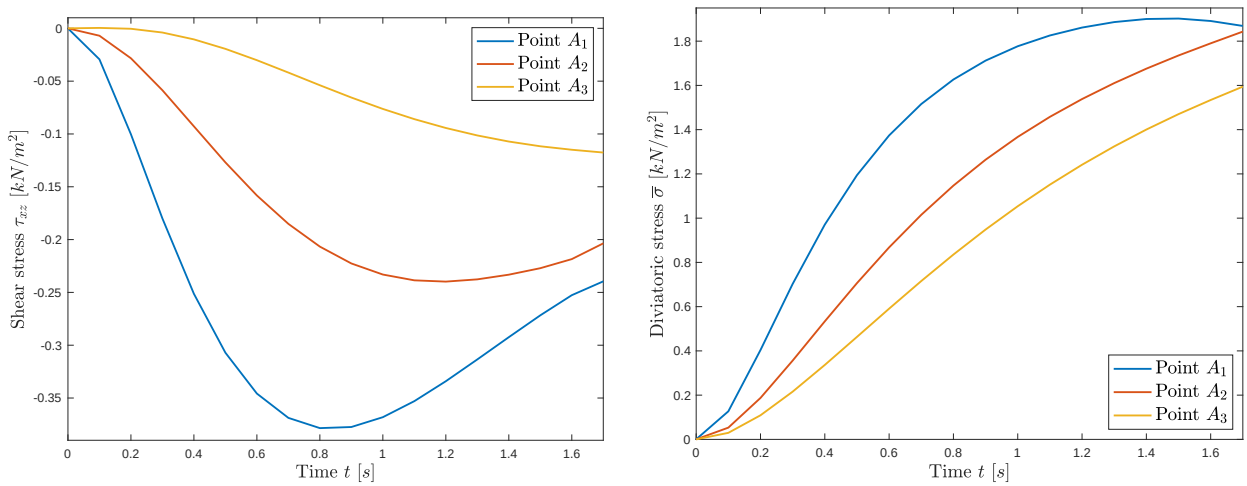

Figure 12: Time evolution of the shear stress τ_{xz} (left plot) and the deviatoric stress $\overline{\sigma}$ (right plot) obtained at the selected points A_1, A_2 and $A3$ for the problem of stresses induced by the dam-break problem over erodible bed.

Table 4: Mesh statistics and obtained results for stresses induced by the overtopping flow over a dyke at time $t = 30$ s. The CPU times are given in minutes.

	# elements	# nodes	max (Z)	max (σ_z)	max (σ_x)	max (τ_{xz})	max $(\overline{\sigma})$	CPU time
Mesh A	942	1995	0.7693	119.8	116.7	80.1	120.6	1.1
Mesh B	1882	3817	0.8425	138.9	139.7	89.5	141.9	2.5
Mesh C	3694	6711	0.9158	142.3	142.8	94.2	144.8	5.3
Mesh D	7406	15149	0.9304	145.8	150.0	96.7	150.9	12.4
Reference	37030	75745	0.9412	146.7	151.7	98.5	155.3	108.6

both stresses also reflect directions such that effects of the deposition in the upper direction are higher than effects of erosion in the lower direction.

To further evaluate the performance of the proposed coupled model in resolving the stresses in this sediment transport problem, we present in Figure 19 the time evolution of the shear and deviatoric stresses at three different points B_1, B_2 and B_3 located at different depth in the computational domain with coordinates $(16.5, -2)$, $(16.5, -3)$ and $(16.5, -4)$, respectively. It is clear that the highest deviatoric stresses are obtained at the gauge B_1 which is the nearest to the deformed bed surface whereas the lowest stresses are detected in the gauge B_3 which is the farest from the bed surface. The shear stresses exhibit different behavior at these gauges during the simulation time. This is expected in sedimentary beds since the shear strength of granular soils increases within the depth because the weight of the overlying material causes an increase in the effective stress on the bed particles. This results in a higher inter-particle friction, which leads to an increase in the shear strength. The proposed coupled model performs well for this stream-flow problem over a trench as the induced stresses are accurately resolved without requiring highly demanding computational resources for the stress analysis of deformable beds.

4.6. Stresses induced by an overtopping flow over a dyke

Our final example consists of the problem of overtopping shallow water flows over erodible beds. It should be noted that this is an example of a complex flow process that includes outburst flow, subcritical flow, supercritical flow, and steady flow. Furthermore, because of the presence of upstream and downstream slopes, effects generated by the bed slope are expected to alter the flow features in this case. Therefore, for risk management, it is also necessary to predict the flow propagation and dyke erosion processes. As a result, this test is being conducted to ensure that the

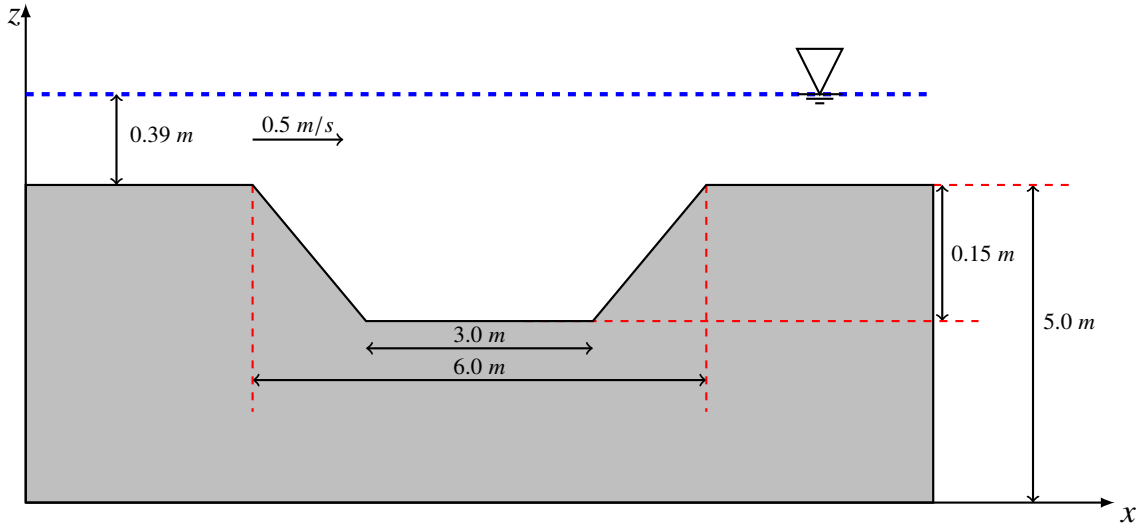

Figure 13: Illustration of the geometry and initial conditions implemented for the problem of stresses induced by the stream-flow problem over a trench.

suggested model system can solve this sediment transport problem under complex hydraulic conditions while also predicting morphological changes. In this example, we consider the experimental setup carried out in [43]. Thus, a dyke is located in the middle of a flume of 35 $m \times 1$ $m \times 1$ m being 0.8 m in height, 1 m wide with a crest width of 0.3 m. Initially, the upstream and downstream slopes of the dyke are 1V:3H and 1V:2.5H, respectively. The dyke is composed of sand with a median diameter of 1.13 mm and the density of 2650 kg/m^3. The erorion term $\mathcal{E}$ and deposition term $\mathcal{D}$ are respectively defined in (9) and (6) with coefficients m and φ defined in (8) and (10), respectively. The bed material porosity is 0.35 and the inflow discharge has a constant value of 1.42×10^{-3} m^3/s. The initial reservoir level is 0.83 m and the downstream water level is 0.03 m. The spatial domain is discretized in 200 control volumes and numerical results are displayed at two different instants $t = 30$ s and $t = 60$ s. The comparison between the numerical results and experimental data at the two considered times is shown in Figure 20. It is clear that the agreement between the numerical simulations and experimental measurements in this figure is fairly good. In fact, profiles of the erodible dyke are well predicted by the proposed numerical approach. Obviously, the computed results for the bed verify the stability and the shock capturing properties of the well-balanced finite volume method. Overall, at $t = 30$ s, the model predicts a bed profile in good matching with the measured results and a reasonably good agreement is also achieved at $t = 60$ s, but a discrepancy is observed at the top of the dyke as a scour hole occurs in the observation, yet this area is smooth in the numerical result and more severe scour is simulated at the downstream of the dyke crest.

Next, we turn our attention to investigate the stresses induced by this problem of stresses induced by an overtopping flow over a dyke accounting for erosion and deposition effects. For this end, a mesh convergence study is first carried out using a series of unstructured meshes with different numbers of nodes and elements as shown in Figure 21. As in the previous example and in order to avoid refining the mesh everywhere in the computational domain, only the area subject to the deformation is refined in these meshes. The corresponding statistics of nodes and elements in each mesh along with the computational results obtained at time $t = 30$ s for the maximum deformation $\max(Z)$ and maximum stresses $\max(\sigma_z)$, $\max(\sigma_x)$, $\max(\tau_{xz})$ and $\max(\overline{\sigma})$ and the CPU times are presented in Table 4. The obtained results of the bed profiles at time $t = 30$ s are displayed in Figure 20 using the considered meshes along with the profile obtained using the reference mesh. Large differences are clearly detected between results obtained using the coarse meshes Mesh A and Mesh B and results obtained using the reference mesh. Refining the density of the elements in the meshes Mesh C and Mesh D generate similar bed profiles and the difference between results obtained on Mesh D and reference mesh becomes negligibly small. These observations can also be seen in the quantitative results summarized in Table 4 but with an increase in the computational cost as the mesh is refined in the simulations. Taking all this into account, a balance between accuracy and efficiency would benefit the Mesh D and therefore this mesh is used in the rest of our computations of stresses induced by this problem of overtopping flow over a dyke.

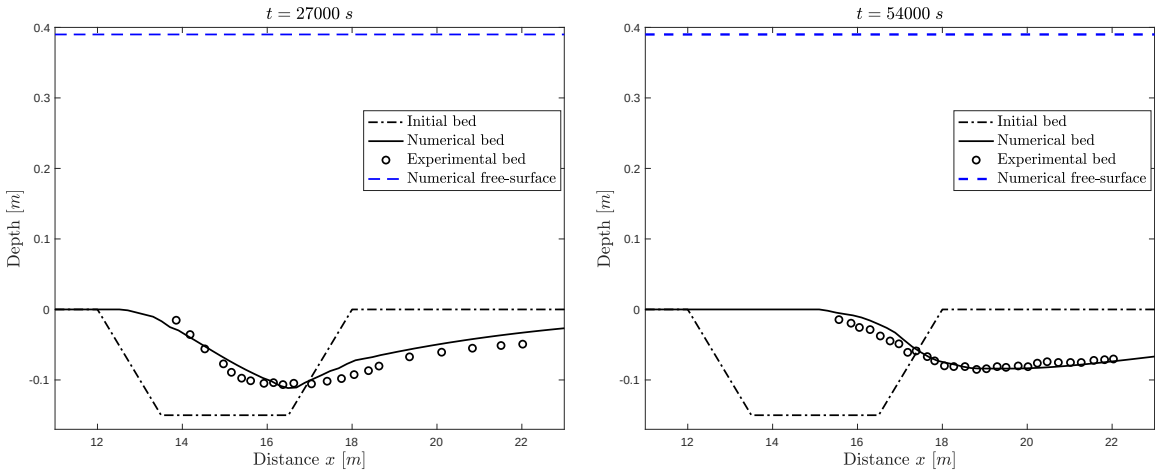

Figure 14: Comparison between experimental results presented in [43] and numerical results obtained using the well-balanced finite volume method solving the stream-flow problem over a trench at time t = 7.5 *hr* (left plot) and t = 15 *hr* (right plot).

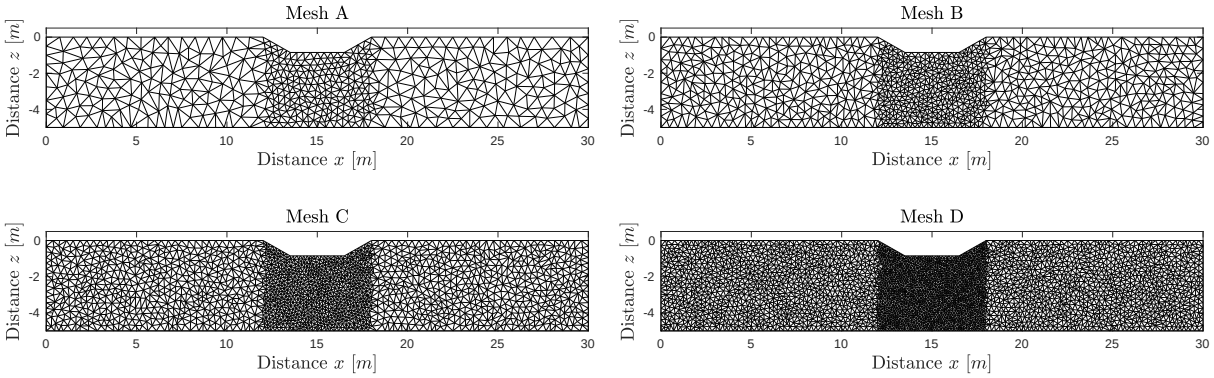

Figure 15: Meshes used in the simulation of stresses induced by the stream-flow problem over a trench.

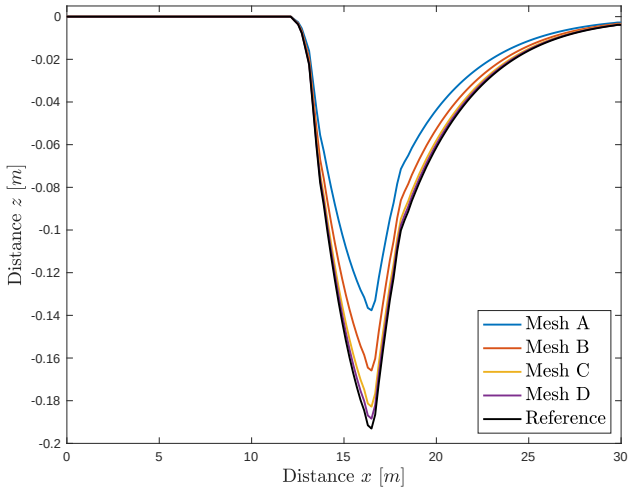

Figure 16: Comparison of bed profiles obtained for the problem of stresses induced by the stream-flow problem over a trench at time $t = 7.5$ hrs.

Table 5: Percentage of the computational cost used by each stage of the coupled simulation, using the time for the first 10 steps. The CPU times are given in seconds.

		Mesh B		Mesh D	
Stage	Algorithm	CPU	Percentage	CPU	Percentage
Sediment stage	Fluxes	0.00327	88.62%	0.01593	88.01%
	RK3	0.00042	11.38%	0.00215	11.99%
	Total	0.00369	100%	0.01810	100%
Stresses stage	Assemblage	0.0072	0.23%	0.0248	0.29%
	Solver	3.1071	99.77%	8.5192	99.71%
	Total	3.1143	100%	8.5440	100%
Total		3.1180	100%	8.5621	100%

In Figure 23 we depict snapshots of the two normal stresses σ_x and σ_z, the shear stress τ_{xz} and the deviatoric stress $\overline{\sigma}$ at time $t = 30$ s. Under the considered sediment transport conditions, the maximum values of stresses are located on the bed topography where the erosion takes place. It is clear that the deformed bed has also been accurately simulated using the proposed hybrid finite volume/finite element method. For instance, the pick of these stress distributions is well resolved and its location is correctly captured for this sediment transport problem. It should also be mentioned that no mesh distortion has been detected in the results obtained for all test examples considered in this study. Finally, Figure 24 exhibits the time evolution of the normal and deviatoric stresses at three different points C_1, C_2 and C_3 located at three different depth with the corresponding coordinates $(20, 0)$, $(20, -0.5)$ and $(20, -1)$, respectively. Again, the high stresses are obtained at the point C_3 and the lowest stresses are at the point C_1. As time evolves, the normal stress σ_z linearly decreases at the selected points in the computational domain. The proposed coupling model performs well for this problem of overtopping flow over a dyke and it accurately captures the induced stresses on a relatively coarse mesh.

Analysis of computational cost has also been carried out in this test example. In Table 5 we summarize the computational cost for simulations using the same parameters as before. Here, the computational cost is divided into two stages: The first stage is the sediment transport stage which involves solving the system (1). This includes Fluxes, representing the percentage of CPU time used for reconstructing the numerical fluxes in the solution of sediment transport equations. RK3, indicating the CPU time allocated for advancing the sediment transport in time. The second stage

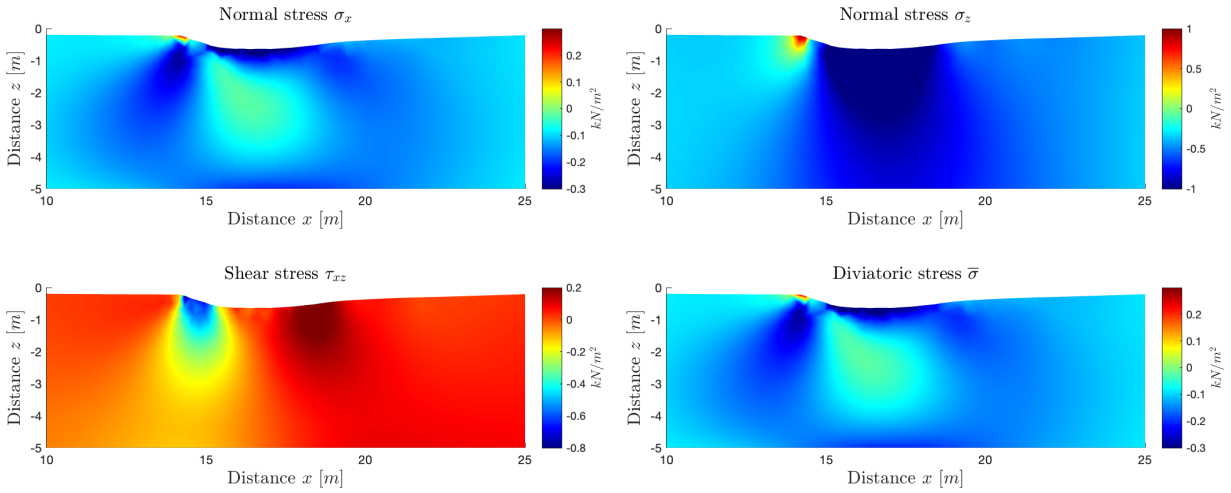

Figure 17: Snapshots of normal stresses σ_x and σ_z, shear stress τ_{xz} and deviatoric stress $\overline{\sigma}$ for the problem of stresses induced by induced by the stream-flow problem over a trench at time $t = 7.5hrs$.

focuses on solving the elastostatic equations (15), referred to as the stresses stage. This includes assemblage, representing the percentage of CPU time used for assembling vectors and matrices in the solution of the linear elasticity problem. Solver, indicating the CPU time allocated for linear solver. The last column presents the total CPU time for both stages combined. The main features reported in this table are on one hand, the sediment transport step requires less computational cost compared to the CPU time needed for the stresses stage. On the other hand, more computational cost is required for simulations on Mesh D than on Mesh B. This is expected as the model adds more accuracy to the solution by adding more degrees of freedom. As can be seen from Table 5, a considerable computational effort goes into the linear solver solving the associated linear systems of algebraic equations. Therefore, reducing the CPU time in the proposed method can be achieved by constructing more efficient preconditioned iterative solvers for these linear systems.

5. Conclusions

A class of coupled numerical models has been proposed for the modelling and simulation of stress fields induced by shallow water flows on movable beds. A hyperbolic system of four equations for balance laws with source terms is employed for modelling combined hydrodynamics, morphodynamics, and suspended sediments. The linear equations of elasticity are employed for the stress analysis in the bed topography. To close the system of governing equations, well-established empirical formulae for the entrainment and deposition terms are implemented, along with linear constitutive relations for stress and strain tensors. The coupling transfer conditions between the two models are achieved through the interface between the water body and the bed topography by sampling the applied forces using the hydrostatic pressure and the friction shear stress obtained from the sediment transport system. For the numerical solution we developed a hybrid finite volume/finite element method which combines a well-balanced finite volume scheme for the sediment transport system and an unstructured finite element solver for the stress analysis. We have also considered a consistent treatment of wet/dry fronts along with a semi-implicit time integration of the bed friction in wet/dry control volumes on the interface. The proposed algorithm satisfies the conservation property and achieves excellent numerical balance between the gradient fluxes and the source terms for the coupled system. To examine the performance of the designed models we have simulated three well-established benchmarks of sediment transport problems. We have compared computational results to experimental data for the bed profiles and we also performed stress analysis in the associated sedimentary beds. The results obtained have exhibited accurate predictions of both hydrodynamics and morphodynamics with correct conservation properties and stable representations of stresses in the movable beds. Although we have restricted our numerical simulations to the one-dimensional sediment transport

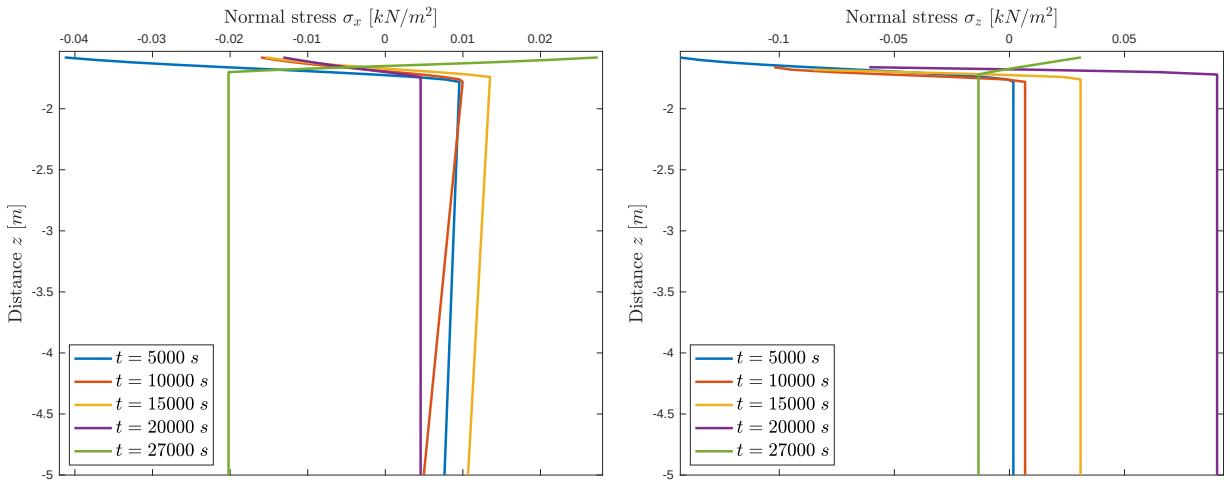

Figure 18: Vertical cross-sections of the normal stresses σ_x (left plot) and σ_z (right plot) obtained at different times for the problem of stresses induced by the stream-flow problem over a trench.

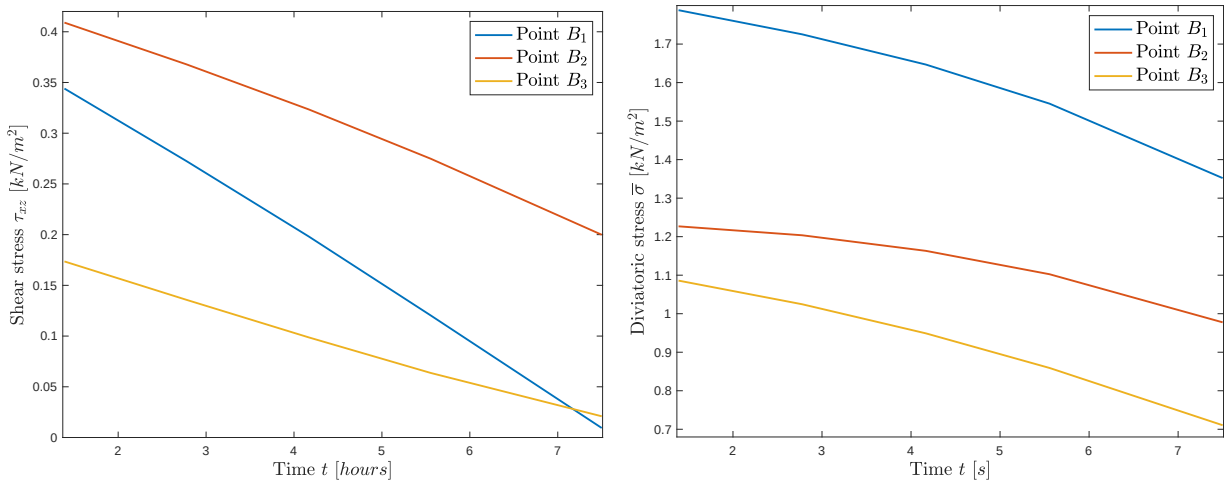

Figure 19: Time evolution of the shear stress τ_{xz} (left plot) and the deviatoric stress $\overline{\sigma}$ (right plot) obtained at the selected points B_1, B_2 and B_3 for the problem of stresses induced by the stream-flow problem over a trench.

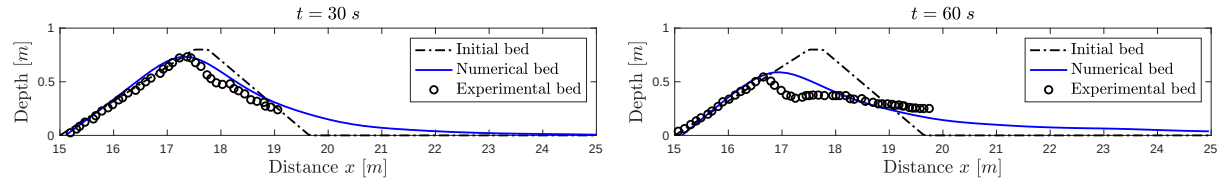

Figure 20: Comparison between numerical results and experimental measurements presented in [43] at time $t = 30$ s (left) and $t = 60$ s (right) for the overtopping flow over a dyke.

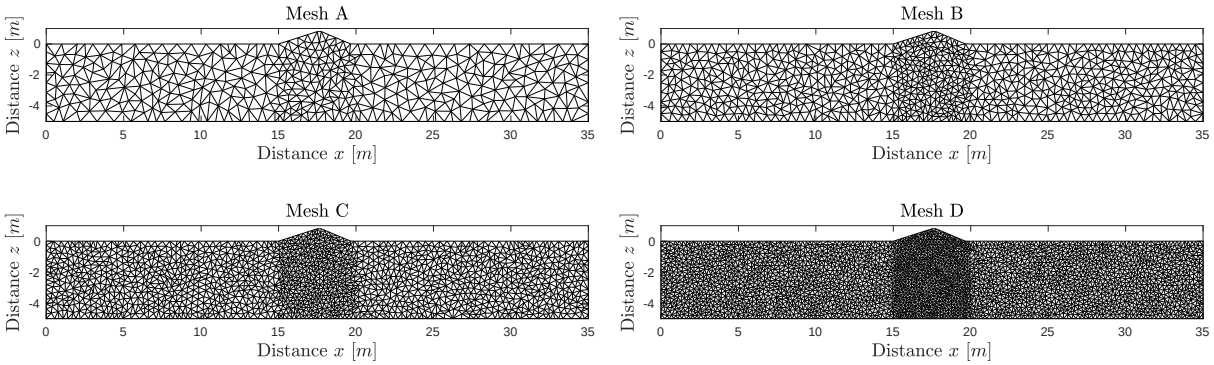

Figure 21: Meshes used in the simulation of stresses induced by the overtopping flow over a dyke.

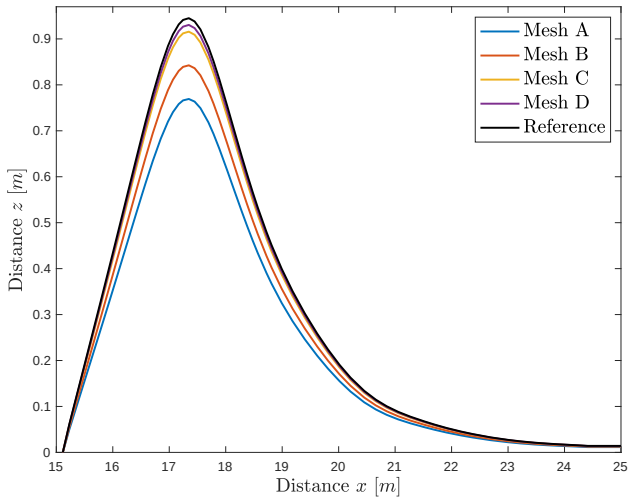

Figure 22: Comparison of bed profiles obtained for the problem of stresses induced by an overtopping flow over a dyke using different meshes at time $t = 30\ s$.

problems, the proposed techniques can be extended to model stress fields induced by shallow water flows over movable beds in two space dimensions accounting for eddy viscosity, wind stresses and Coriolis forces. Furthermore, in many practical problems in geotechnics, the stress-strain equations are not precisely defined by linear constitutive relations. The presence of elastoplasticity in these applications can be conveniently described by nonlinear relations, whose parameters are mainly inferred from experiments. This requires to include, in the governing partial differential equations modelling the problem under study, a rational assessment of plasticity. Developing robust numerical tools for solving these problems is of great interest. Another limitation of the sediment transport model used in the present work is the failure to capture vertical dynamics of the water flow and sediment concentration, and for this class of problems multilayer sediment transport models as those proposed in [44] are needed. In addition, in many sediment transport applications, the bed is formed of different sediments with different material properties and different packing distributions including erodible and non-erodible parts. The proposed approach can still apply for these applications under the condition that a consistent model is used for the sediment transport accounting for heterogeneous beds such as multilayered soils. In this case, a series of erosion and deposition formulae as those introduced in [45, 46] are required for which the sediment transport model switches from one to another according to specific depths within the bed. These and further issues are subject of future investigations. Future works will also be devoted to comparing the resulting stress fields with experimental measurements. This comparison will help to assess how useful this class of

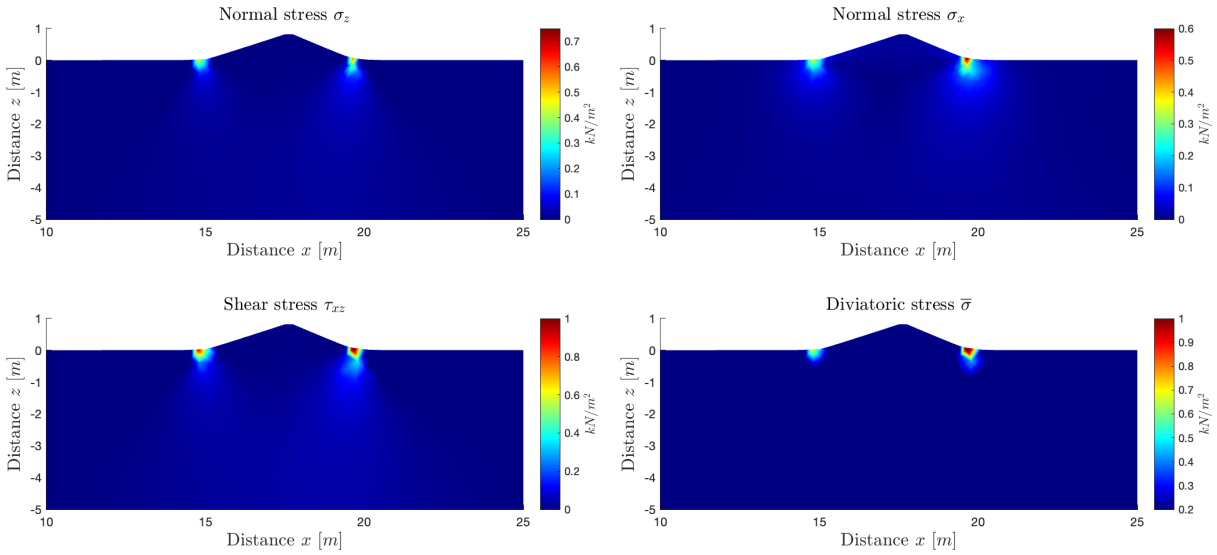

Figure 23: Snapshots of normal stresses σ_x and σ_z, shear stress τ_{xz} and deviatoric stress $\overline{\sigma}$ for the problem of stresses induced by induced by an overtopping flow over a dyke at time $t = 30\ s$.

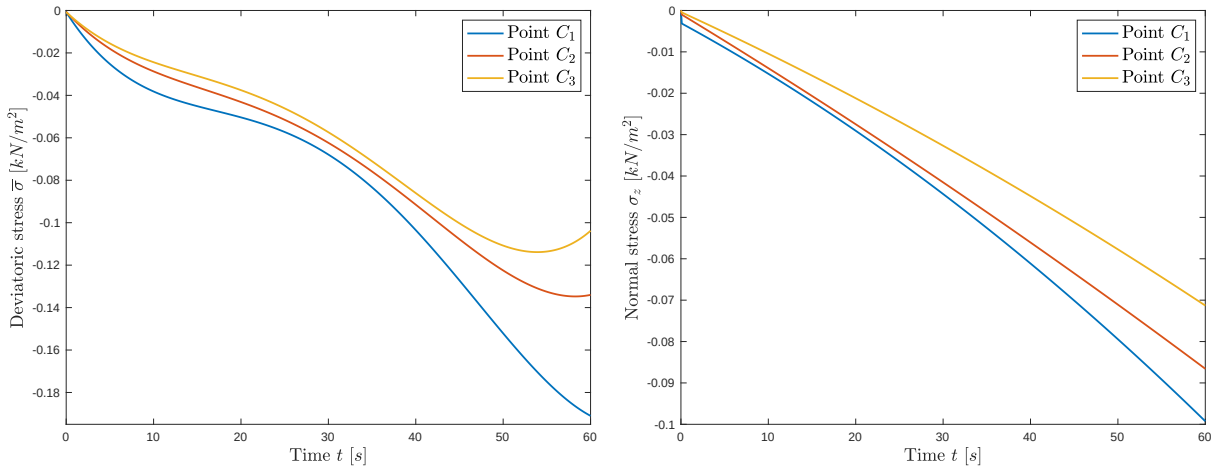

Figure 24: Time evolution of the shear stress τ_{xz} (left plot) and the deviatoric stress $\overline{\sigma}$ (right plot) obtained at the selected points C_1, C_2 and $C3$ for the problem of stresses induced by an overtopping flow over a dyke.

models is at the operational level.

Acknowledgements

This work is funded by the British Council under Newton Fund Institutional Link programme (Grant reference 62309484).

Data availability statement

The data that support the findings of this study are available from the corresponding author upon reasonable request.

Acknowledgment

The authors would like to thank anonymous referees for giving very helpful comments and suggestions that have greatly improved this paper.

References

[1] C. Escalante, T. Luna, M. Castro, Non-hydrostatic pressure shallow flows: GPU implementation using finite volume and finite difference scheme, International Journal for Computer-aided Engineering and Software 338 (2018) 631–659.
[2] R. Acharyya, Evaluation of overall response of driven pile in multi-layered soil, Transportation infrastructure geotechnology 11 (2023) 1–20.
[3] M. Avand, M. Mohammadi, F. Mirchooli, A. Kavian, J. Tiefenbacher, A new approach for smart soil erosion modelling: Integration of empirical and machine-learning models, Environmental modelling assessment 1 (2023) 145–160.
[4] E. Ortega, E. Onate, S. Idelsohn, Method for shallow water equations, International Journal for numerical methods in engineering 88 (2011) 180–204.
[5] A. Waheed, M. Henschke, A. Pfening, Simulating sedimentation of liquid drops, International Journal for numerical methods in engineering 8 (2023) 1–59.
[6] M. Diaz, E. Nieto, A. Ferreiro, Sediment transport models in shallow water equations and numerical approach by high order finite volume methods, Computers and fluid 37 (2008) 299–316.
[7] H. Yu, K. Shen, B. Wu, H. Wei, An experimental study of interaction between bank collapse and riverbed evolution, Advances in water resources 5 (2013) 675–682.
[8] M. Yu, X. Chen, Y. Wei, W. Hu, B. Wu, Experiment of the influence difference near-bank riverbed compositions on bank failure, Advances in water resources 2 (2016) 176–185.
[9] S. Li, C. Duffy, Fully coupled approach to modeling shallow water flows, sediment transport, and bed evolution in rivers, Water resources research 47 (2011) 1–20.
[10] M. Saleh, M. Laman, T. Baran, Experimental determination and numerical analysis of vertical stresses under square footings resting on sand, Digest 19 (2008) 4521–4538.
[11] B. Wu, H. Yu, Experimental study on bank failure process and interaction with riverbed deformation due to fluvial hydraulic force, Journal of hydraulic engineering 6 (2014) 649–657.
[12] L. Cea, J. French, M. Cendon, Numerical modelling of tidal flows in complex estuaries including turbulance: An unstructured finite volume solver and experimental validation, International Journal for numerical methods in engineering 59 (2004) 1821–1837.
[13] D. Lyn, M. Altinakar, St. Venant-Exner equations for near-critical and transcritical flows, Journal of hydraulic engineering 128 (2002) 579–587.
[14] P. Tassi, S. Rheberg, C. Vionnet, O. Bokhove, Discontinuous Galerkin finite element for river bed evolution under shallow flows, Computer method in applied mechanics and engineering 197 (2008) 2930–2947.
[15] S. Soares-Frazao, Y. Zech, HLLC scheme with novel wave-speed estimators appropriate for two-dimensional shallow-water flow erodible bed, International Journal for umerical methods in fluids 66 (2011) 1019–1036.
[16] C. Juez, J. Murillo, P. Garcia-Navarro, A 2D weekly-coupled and efficient numerical model for transient shallow flow and movable bed, Advances in water resources 71 (2014) 93–109.
[17] L. Fraccarallo, H. Capart, Riemann wave description of erosional dam-break flows, Journal of fluid mechanics 461 (2002) 183–228.
[18] M. Ali, M. Seeger, G. Sterk, D. Moore, A unit stream power based sediment transport function for overland flow, Estuarine coastal and shelf science 101 (2013) 197–204.
[19] A. Armstrong, N. Quinton, P. Heng, H. Chandler, Variability of interhill erosion at low slopes, Earth Surface Processes and landforms 36 (2011) 97–106.
[20] J. M. Martínez-Aranda, S., P. García-Navarro, Comparison of new efficient 2D models for the simulation of bedload transport using the augmented Roe approach, Advances in water resources 153 (2021) 1–23.
[21] J. M. Martínez-Aranda, S., P. García-Navarro, A robust two-dimensional model for highly sediment-laden unsteady flows of variable density over movable beds, Journal of hydroinformatics 22 (2020) 1038–1060.
[22] A. Al-Ghosoun, A. Osman, M. Seaid, A computational model for simulation of shallow water waves by elastic deformations in the topography, Communications in Computational Physics 29 (2021) 1095–1124.
[23] A. Al-Ghosoun, A. Osman, M. Seaid, A hybrid finite volume/finite element method for shallow water waves by static deformation on seabeds, Engineering Computations 38 (2021) 2434–2459.
[24] P. Li, A. Tariq, Q. Li, B. Ghaffar, M. Farhan, A. Jamil, Soil erosion assessment by RUSLE model using remote sensing and GIS in an arid zone, International Journals of digital earth 16 (2023) 3105–3124.
[25] Z. Cao, G. Pender, P. Carling, Shallow water hydrodynamic models for hyperconcentrated sediment-laden floods over erodible bed, Advances in water resources 29 (2006) 546–557.
[26] Z. Cao, G. Pender, S. Wallis, P. Carling, Computational dam-break hydraulics over erodible sediment bed, Journal of hydraulic engineering 67 (2004) 689–703.
[27] F. Benkhaldoun, S. Sari, M. Seaid, A flux-limiter method for dam-break flows over erodible sediment beds, Applied mathematical modelling 36 (2012) 4847–4861.
[28] Z. Cao, P. Carling, Mathematical modelling of alluvial rivers: reality and myth. part I: General overview, Water Maritime Engineering 154 (2002) 207–220.
[29] F. Benkhaldoun, S. Sari, M. Seaid, Computational dam-break hydraulics over erodible sediment bed, Applied mathematical modelling 36 (2012) 4847–4861.

[30] W. Wu, D. Virria, S. Wang, One dimensional modeling of dam-break flows over erodible beds, Journal of hydraulic engineering 130 (2004) 914–923.
[31] M. Elhakeem, J. Imran, Density functions for entrainment and deposition rates of uniform sediment, Journal of hydrology 133 (2007) 917–926.
[32] M. Garcia, G. Parker, Enterainment of bed sediment into suspension, Journal of hydraulic engineering 117 (1991) 414–435.
[33] Z. Cao, Equillibrium near-bed concentration of suspended sediment, Journal of hydraulic engineering 125 (1999) 1270–1278.
[34] B. Reddy, M. Kussner, Some low-order quadrilateral elements based on novel integration rules, Engineering computations 15 (1998) 700–720.
[35] S. Bunya, E. Kubatko, J. Westerink, C. Dawson, A wetting and drying treatment for Runge-Kutta discontinuous Galerkin solution to the shallow water equations., Computer methods in applied mechanics and engineering 198 (2009) 1548–1562.
[36] S. Gottlieb, D. Ketcheson, C.-W. Shu, Strong stability preserving Runge-Kutta and multistep time discretizations, World Scientific, 2011.
[37] M. Pastor, M. Herreros, J. Merodo, Numerical modelling of the propagation of fast landslide using the finite element method, International Journal for numerical methods in engineering 59 (2004) 755–794.
[38] K. Sairajan, S. Deshpande, M. Patnaik, D. Poomani, Base force and moment based finite element model correlation method, Advances in space research 68 (2021) 4056–4068.
[39] A. Hudson, P. Sweby, Formations for numerically approximating hyperbolic systems governing sediment transport, Journal of scientific computing 19 (2003) 225–252.
[40] J. Aguirre, M. Castro, T. Luna, A robust model for rapidly varying flows over movable bottom with suspended and bedload transport: modelling and numerical approach, Advances in water resources 140 (2020) 1–22.
[41] C. Juez, J. Murillo, P. Garcia-Navarro, One-dimensional Riemann solver involving variable horizontal density to compute unsteady sediment transport, Journal of Hydraulic Engineering 142 (2015) 1–16.
[42] J. Boussinesq, Application des potentiels a l'etude de l'equilbre et du movement des solids elastiques, Gauthier-Villars (1885).
[43] M. Guan, N. Wright, A. Sleigh, Multimode morphodynamic model for sediment-laden flows and geomorphic impacts, Journal of hydraulic engineering 141 (2015) 1–23.
[44] T. Rowan, M. Seaid, A multilayered shallow water model for sediment transport in flows over heterogeneous erodible beds, The European Physical Journal Plus 137 (8) (2022) 974.
[45] T. Rowan, M. Seaid, Efficient computational models for shallow water flows over multilayer erodible beds, Engineering Computations 37 (2) (2019) 401–429.
[46] T. Rowan, M. Seaid, Two-dimensional numerical modelling of shallow water flows over multilayer movable beds, Applied Mathematical Modelling 88 (2020) 474–497.

Durham University
Durham Research Online

Citation on deposit: Al-Ghosoun, A., Seaid, M., & Osman, A. S. (2025). A novel approach for modelling stress fields induced by shallow water flows on movable beds. Applied Mathematical Modelling, 142, Article 115960. https://doi.org/10.1016/j.apm.2025.115960

For final citation and metadata, visit Durham Research Online URL:
https://durham-repository.worktribe.com/output/3351587

Copyright statement: This accepted manuscript is licensed under the Creative Commons Attribution 4.0 licence.
https://creativecommons.org/licenses/by/4.0/